Acoustic emission approach for identifying fracture mechanisms in composite bonded Joints

A study on varying Substrate's stacking sequence

Lima, R. A.A.; Tao, R.; Bernasconi, A.; Carboni, M.; Teixeira de Freitas, S.

DOI
10.1016/j.tafmec.2024.104490

Publication date
2024

Document Version
Final published version

Published in
Theoretical and Applied Fracture Mechanics

Citation (APA)
Lima, R. A. A., Tao, R., Bernasconi, A., Carboni, M., & Teixeira de Freitas, S. (2024). Acoustic emission approach for identifying fracture mechanisms in composite bonded Joints: A study on varying Substrate's stacking sequence. *Theoretical and Applied Fracture Mechanics*, *132*, Article 104490. https://doi.org/10.1016/j.tafmec.2024.104490

Theoretical and Applied Fracture Mechanics 132 (2024) 104490

Contents lists available at ScienceDirect

Theoretical and Applied Fracture Mechanics

journal homepage: www.elsevier.com/locate/tafmec

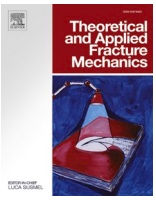

Acoustic emission approach for identifying fracture mechanisms in composite bonded Joints: A study on varying Substrate's stacking sequence

R.A.A. Lima [a,b,*], R. Tao [b], A. Bernasconi [a], M. Carboni [a], S. Teixeira de Freitas [b,c,*]

[a] Department of Mechanical Engineering, Politecnico di Milano – Milan, Italy
[b] Aerospace Structures and Materials, Faculty of Aerospace Engineering, Delft University of Technology – Delft, Netherlands
[c] IDMEC, Instituto Superior Técnico, Universidade de Lisboa, Lisboa, Portugal

ARTICLE INFO

Keywords:
Secondary adhesive bonded joints
CFRP layup tailoring
Acoustic emission
Toughening mechanisms
Artificial neural network

ABSTRACT

This study uses the acoustic emission structural health monitoring method to identify fracture mechanisms in composite bonded joints when varying the substrate stacking sequence. Quasi-static mode I loading tests were performed on secondary adhesively bonded multidirectional composite substrates (0, 90, 45, −45, 60 and −60° fibre orientations). An unsupervised artificial neural network combined with the visual fracture evaluation of the specimens and the Morlet continuous wavelet transform was used to cluster and give the acoustic emission signals a physical meaning. Different fracture mechanisms could be identified within the adhesive layer (i.e., cohesive failure) and in the composite substrates, including non-visible damage mechanisms (matrix micro-cracking, fibre/matrix debonding, fibre pull-out and fibre breakage). Using the Morlet continuous wavelet transform, it was possible to recognise that the highest peak frequency does not always represent the most relevant signature of the fracture mechanism. Moreover, multiple peak frequencies can be associated with multiple fracture mechanisms, such as the fibre pull-out that occurs in the combination of matrix cracking and fibre breakage. Furthermore, no differences were observed in mode I loading conditions between the acoustic emission signatures from the cohesive failure in the adhesive layer and the matrix cracking within the composite substrate. The findings of this study present a great opportunity to gain more insight into the fracture behaviour of polymer materials and fibre-reinforced polymer materials and to improve the quality of adhesively bonded joints.

1. Introduction

The use of composite adhesively bonded joints is increasing in most industrial fields, mainly in the transportation segment, due to its main advantages as lightweight design versatility of the components and minimal impact on the substrates' mechanical properties [1–3]. However, in the aeronautical industry, secondary bonded joints of primary structures are not yet certified. Consequently, backup solutions such as rivets and bolts must be applied to increase the bonded component's safety and avoid catastrophic failures [3–7].

A thorough understanding of the damage mechanisms and fracture resistance of composite adhesively bonded joints will help to address key challenges to increase the safety and damage tolerance of secondary bonded joints in high load-bearing structures, avoid overdesign and improve the joints' reliability and resistance against sudden failure (improve fracture toughness) [3,6,8–13].

Previous research has shown that tailoring the substrates composite stacking sequence can increase the joints' fracture toughness [1,14,15], in which different toughening mechanisms (intrinsic and extrinsic) can be simultaneously triggered, affecting crack propagation paths and, in some cases, delaying crack advancement.

Furthermore, Non Destructive Testing (NDT) and Structural Health Monitoring (SHM) techniques can be applied to verify the bonded structures' integrity and increase their reliability [8,16–22]. In particular, SHM methods can be used for real-time or on-demand monitoring of the joints during their operational life, identifying and locating critical events [23]. Among the various SHM methods, Acoustic Emission (AE) can also provide valuable information about the type of damage mechanisms progressing within the composite substrates and in adhesively bonded joints [24–33] since it can assess the ultrasonic elastic waves produced when strain energy is spontaneously released due to straining or damage evolution [24].

* Corresponding authors.
E-mail addresses: R.DeAraujoAlvesLima@tudelft.nl (R.A.A. Lima), sofia.teixeira.freitas@tecnico.ulisboa.pt (S. Teixeira de Freitas).

https://doi.org/10.1016/j.tafmec.2024.104490
Received 13 February 2024; Received in revised form 24 May 2024; Accepted 24 May 2024
Available online 27 May 2024

Many researchers used the AE method for damage characterisation within unidirectional and woven-based composite materials [26,27,29,32,34–39] by associating the differences of the features of AE signals in the time and frequency domain with the damage mechanisms observed by different experimental techniques (visual inspection, ultrasonic guided waves, Digital Image Correlation – DIC – and strain sensing by optical fibres). Nevertheless, few works considered the effects of different ply orientations in the assessed AE waveforms obtained from composite bonded joints [40–42].

W. Li *et al.* [40] used the AE method combined with micro visualisation (microscopy images) to identify different damage mechanisms of carbon fibre-reinforced polymer (CFRP) composite multidirectional laminates with interface orientations of 0, 30, 45 and 60°. The authors could find a direct relationship between the AE features (particularly the Rise Angle) with the damage initiation and classification, accurately identifying the beginning of the delamination in the studied composites. It is worth mentioning that no adhesive layer was present in this research, and only visible damage mechanisms could be identified.

Kupski *et al.* [42] studied the effects of different composite layups on the failure mechanisms of single-lap bonded joints. The AE monitoring was used to give only a general overview of the cumulative hits during the tests and identify total damage accumulation through Sentry function analysis. There was no deeper analysis correlating the AE waveforms and the various damage mechanisms observed during the tests.

For secondary adhesively bonded joints with increased complexity due to the tailored design of the composites' substrates, there is a lack of knowledge on how toughening mechanisms are triggered and how multi-damage mechanisms impact the joints' fracture toughness and damage tolerance design. The authors strongly believe that a monitoring technique such as acoustic emission combined with in-depth data analysis can provide meaningful information on the several failure mechanisms triggered by the different composite stacking sequences and their competition with crack development in the adhesive layer, helping a deeper understanding of the damage evolution.

Therefore, this research paper investigates how the bondline in adhesively bonded CFRP multidirectional laminates (0, 90, 45, −45, 60 and −60° fibre orientations) can affect the identification of damage mechanisms using AE data and how AE data can help further understand the damage mechanisms present. Moreover, the feasibility of the AE method in identifying the co-occurrence of various visible and non-visible damages (i.e. matrix/fibre debonding and fibre pull-out) in tailored adhesively bonded joints is addressed.

2. Materials

The composite substrates of the DCB specimens were manufactured using the unidirectional carbon fibre prepregs Hexply 8552 – AS4 toughened epoxy resin (Hexcel Composites, from Cambridge – U.K.) [43]. The following layups were manufactured: $[0]_8$, $[0/90_2/0]_S$, $[90/0_2/90]_S$, $[90/45/-45/0]_S$, $[90/60/90/-60/0]_S$. The substrates were bonded using AF163 – 2 K toughened epoxy adhesive with an embedded carrier ($G_{IC} = 2416$ J/m^2 [44]) supplied by 3 M Scotch Weld^{TM}, Delft – The Netherlands. More details about the materials' properties can be found in [14].

Pure CFRP specimens $[0]_{16}$, with a Teflon insert (thickness equal to 0.01 mm) embedded between ply 8 and 9 of the composite to introduce a crack initiation, were also produced to capture the acoustic emission data from laminates without an adhesive layer.

2.1. Specimens manufacturing

A hand layup method was used to produce the substrate's stacking sequence. Debulking steps were applied at each added CFRP ply in a sealed table under a constant pressure of around 100 mbar for 20 min. After that, the CFRP laminates were placed on an aluminium plate covered with an A4000 high-performance fluoropolymer release film (Airtech International INC, USA), and a vacuum bag was built to keep the specimens under pressure. Finally, the substrates were polymerised in an autoclave under 7 bars of pressure and 110 °C for 60 min.

Once cured, the smooth surface of the substrates (previously on the side of the aluminium plate) was manually sanded following a criss-cross pattern using 400-grid sandpaper. Afterwards, a degreasing step with a soaked acetone cloth was performed. Then, the cleaned surfaces were exposed to artificial high-intensity U.V. lights (wavelengths of 184.9 nm and 253.7 nm) with a working treatment distance (between lamps and specimens) of 40 mm for 7 min in a U.V./Ozone in-house apparatus. This physical treatment aimed to remove the remaining thin layer of organic contaminations by their decomposition in volatile substances and, finally, improve their wettability angles, as shown in [44,45].

The adhesive film was applied to the treated surface immediately after removing the substrate's plates from the U.V./Ozone apparatus. Firstly, a Teflon tape (total thickness of 0.11 mm) was attached to the beginning of the substrate to create the initial crack length ($a_0 = 30 \pm 1$mm) and help to keep the adhesive thickness constant through the specimen's length. Then, the adhesive film was applied to the free-cleaned surface. An even thickness of the adhesive layer equals to 0.25 mm was ensured due to its embedded carrier. Finally, the joints were cured in the autoclave for 90 min at 120 °C and 3 bar.

After the adhesive curing cycle, the joints were cut at the correct dimensions of the DCB specimens (see the schematic of Fig. 1) using the PROTH (PROTH Industrial Co. Ltda, Taiwan) cutting/gridding machine with a diamond saw. Loading blocks were bonded at their up and bottom surfaces using a bi-component epoxy adhesive Araldite 2012.

Table 1 shows the nomenclature used during the manuscript for each specimen type. At least four specimens of each stacking sequence were tested.

3. Experimental set-up (DCB)

The DCB quasi-static displacement-controlled tests were performed in a Zwick electro-mechanical testing machine with a 1 kN load cell and a 4 mm/min testing speed, according to ISO 25217 standard. The load and displacement values were recorded with a 10 Hz sampling frequency.

It is worth mentioning that no pre-cracking stage was performed since this might influence the assessment of the crack competition phenomena due to their early occurrence in the fracture, as detailed in [14]. Because of this, the initial crack tip geometry is closer to a weak or kissing bond than with a sharp crack.

During the tests, the crack position was tracked with a digital camera (resolution of 4 M pixels), distant 60 mm from the white-painted lateral side of each specimen. A travelling microscope also captured the crack propagation paths from the specimen's free lateral side. The travelling microscope lens was positioned around 5 mm from the speciemen's surface. The digital camera and microscope presented four photos per second acquisition frequency. An ex-situ X-ray micro CT scanner (Phoenix Nanotom, Waygate Technologies, Germany) was used in some specific specimens to visualise the damage mechanisms further. Before scanning, the selected DCB samples were loaded, and a metallic insert was used to keep the opening arms fixed during ex-situ analysis. The resulting 3D model had a voxel size of 12.5 μm.

A single Vallen VS900-M broad frequency piezoelectric resonant transducer sensor (resonant working frequency between 100–900 kHz) linked with a 34 dB AEP5 pre-amplifier connected to the 4-channel Vallen ASMY-6 acquisition unit (Vallen Systeme GmbH, Icking, Germany), through low-noise cables, was used for the acoustic emission acquisition set-up. The Vallen AE-suite R2019.0926.1 software was used to manage and set the main parameters for data acquisition (see Table 2). The AE data acquisition was synchronised with the load and displacement values from the testing machine, allowing their direct correlation with the AE events.

The Magnaflux Ultragel II was used as a high-performance coupling

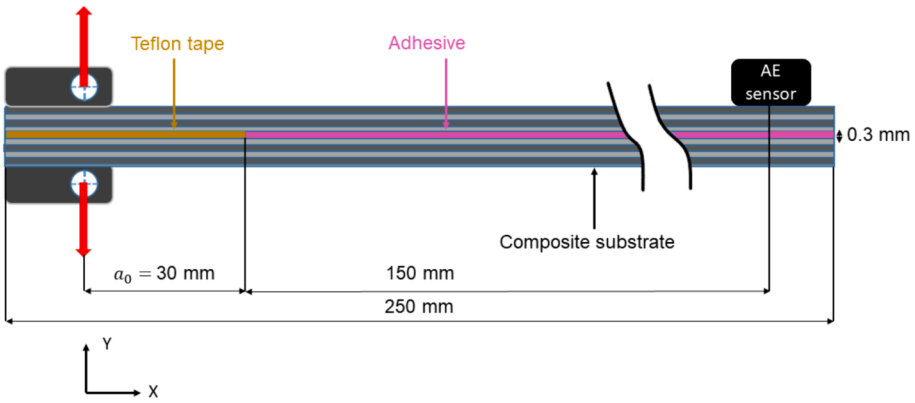

Fig. 1. Schematic of DCB specimen dimensions (out of scale) – specimen's width of 25 mm.

Table 1
Type of specimens tested.

Nomenclature	Adhesive	Stacking sequence	Specimen's total thickness [mm] Average ± standard deviation
CFRP	–	$[0]_{16}$	2.38 ± 0.04
AF-0	AF163-2 k	$[0]_8$	2.60 ± 0.02
AF-0/90	AF163-2 k	$[0/90_2/0]_S$	2.57 ± 0.02
AF-90/0	AF163-2 k	$[90/0_2/90]_S$	2.58 ± 0.04
AF-90/45	AF163-2 k	$[90/45/-45/0]_S$	2.43 ± 0.06
AF-90/60	AF163-2 k	$[90/60/90/-60/0]_S$	2.87 ± 0.04

Table 2
AE acquisition parameters.

Amplitude threshold (to a reference voltage amplitude of 1 μV)	40 dB
Sampling rate for the acquisition of the AE features	10 MHz
Sampling rate for the acquisitions of AE waveforms	2 MHz
Minimum frequency of acquisition	25 kHz
Rearm time	400 μs
Duration discrimination time (time window to register each AE signal)	400 μs
Pre-trigger time	200 μs
Digital pass-band filter	25-850 kHz

agent to guarantee the continuity of the AE signals transmission from the material's external surface and the sensor itself. The sensor was placed 150 mm from the joint's initial crack length and maintained in position by a mechanical clamp. The testing set-up is shown in Fig. 2.

It is worth mentioning that the Hsu-Nielsen test [46] was performed to aid in defining the main acquisition parameters to be used during the DCB tests and evaluate the optimal distance to position the sensor, avoiding high attenuation. It is important to note that setting the correct amplitude threshold is crucial for acquiring AE data. Hence, an initial acquisition was performed without conducting the mechanical test to identify amplitude values related to environmental noise [33] and, finally, the threshold value was set to 40 dB.

4. AE data and post-processing

Various time-domain features can be directly extracted from the acoustic emission data, such as: amplitude, counts (the number of times the waveform crosses the acquisition threshold line), energy (area under the squared signal envelope measured in [eu] – one "energy unit" equals to 10^{-18} J); duration (total time from the first and last time that the waveform crosses the threshold line); rise-time (time from the first time that the waveform crosses the threshold line until the maximum amplitude value); and Root Mean Square (RMS) of the amplitude values of each AE source. Some of them are defined in Fig. 3.

The waveforms of the AE data were also recorded, and a Fast Fourier Transform (FFT) was applied to determine the AE waveforms' variance, peak and centroid frequencies [24,47]. It is worth noting that some reflections and almost simultaneous signals can be recorded in the same waveform for a given duration discrimination time. However, they will only be considered for energy determination if continuous and above the recording threshold.

After each DCB test, the recorded acoustic emission data were filtered. All the data with the number of counts equal to or less than two were considered background noise and eliminated. Fig. 4 shows one example of the AE data remaining after filtering along the load–displacement curve (black curve) for the specimen AF-0.

As can be observed in Fig. 4, the primary acoustic emission sources happen at the crack propagation stage of the tests (after the maximum load peak). Nevertheless, AE activity is still recorded at the initial stage of the test (increasing loading values until the maximum load is reached), probably indicating some damage initiation but not critical enough to propagate a main crack path. The raw data from the remaining AE tests can be found in Appendix A. A similar behaviour is observed.

Fig. 5 shows the energy and count values of the acoustic emission sources for the AF-0 representative specimen type. Similar plots for the remaining specimen types can be found in Appendix B.

Analysing the evolution of energy and count values during the test is a practical qualitative way to understand each specimen's behaviour, how the damage accumulates during the tests, and when the most energetic waveforms were generated. However, it is insufficient to make a quantitative analysis to compare different stacking sequences [24].

Furthermore, each specimen configuration studied here presents multi-complex fracture mechanisms, as detailed in [14], which cannot always be observed from the lateral side images taken during the tests.

Hence, to make a deeper interpretation of the AE data, an accurate clustering of the acoustic emission data and attribution of physical meaning to each cluster is crucial to a better understanding of when these damage mechanisms were triggered and developed. The applied clustering methodology is described in the following sections.

4.1. Principal component analysis (PCA) and clustering methodology

Fig. 6 shows the clustering methodology scheme used for all the AE data analysed.

As seen in Fig. 6, once the set of AE features is extracted, choosing the most relevant features and separating the data into groups is crucial for clustering success [48–50]. Accordingly, the Principal Component Analysis (PCA) was proposed [51].

The PCA is a widely used multivariable method to reduce the dimensionality of large datasets and improve their visualisation by projecting the data in the direction that maximises their variance. The

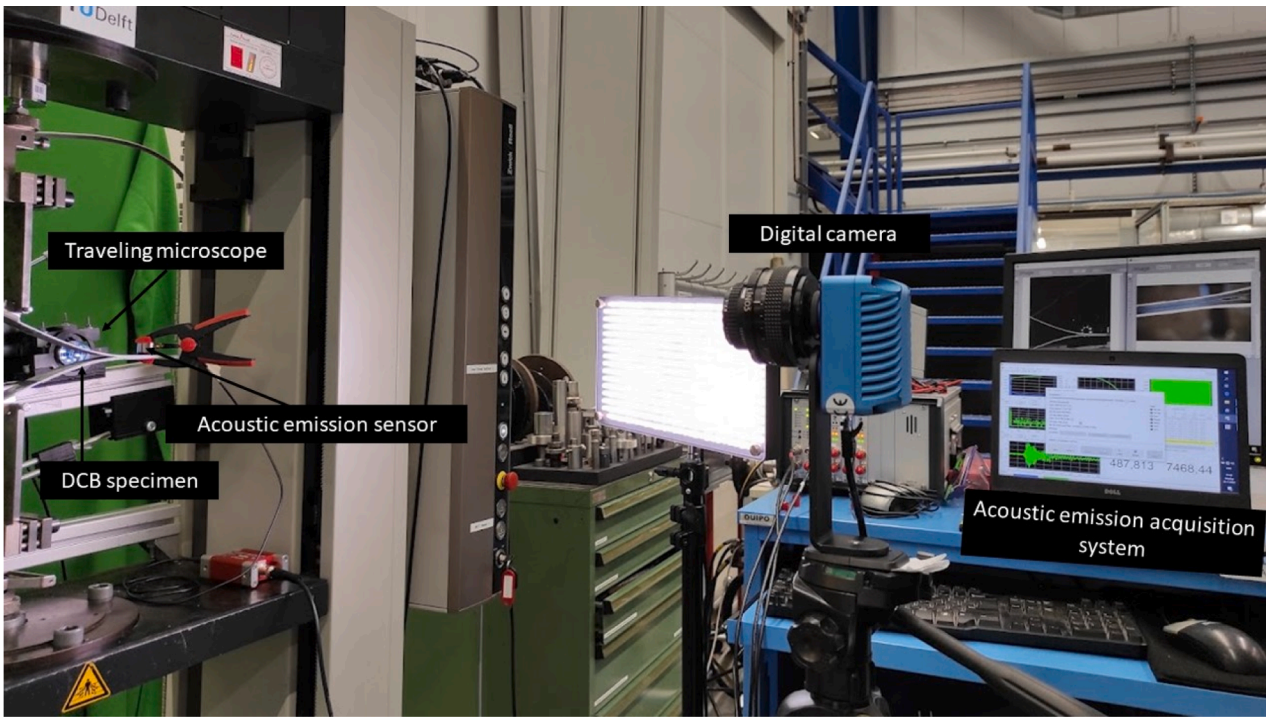

(a)

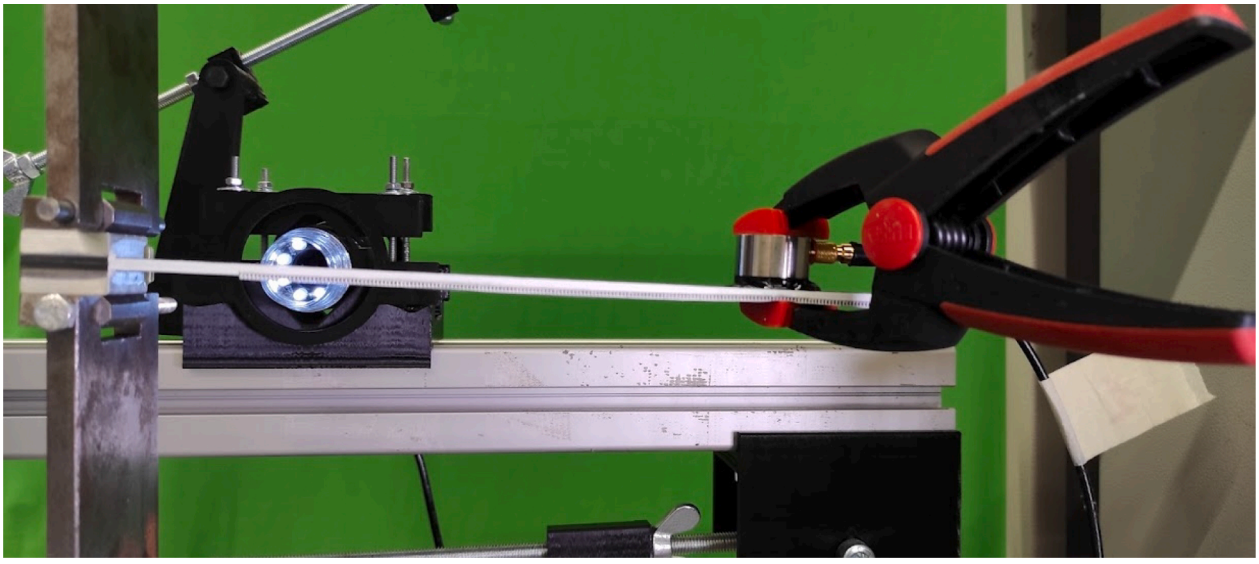

(b)

Fig. 2. (a) Experimental set-up DCB testing and (b) detail of the DCB specimen and acoustic emission sensor.

covariance matrix of the eight selected features (amplitude, energy, counts, duration, rise-time, variance, peak frequency and centroid frequency), their eigenvalues, eigenvectors, and contribution rate were calculated.

In order to determine the optimal number of principal components, cumulative contribution rates greater than 80 % were considered. Finally, the energy and peak frequency features were selected as primary input values for the unsupervised Artificial Neural Network (ANN) since they present a higher contribution for the variance captured by the principal components; see the graph of step 3 in Fig. 6, presenting an average cumulative contribution rate of 98 %.

Since the acoustic emission data was not previously labelled, an unsupervised ANN methodology based on the Self-Organising Map (SOM) was selected [25,27,52]. Fig. 6 shows the clustering methodology scheme used for all the AE data analysed.

The SOM training algorithm is based on organising the input data (also called neurons) into a 2D topological map (U-matrix) that classifies them according to their similarities based on their relative Euclidean distance by using neighbourhood functions – step 4 in Fig. 6.

The k-means interactive algorithm [53] was used to cluster the U-matrix by considering a range of possible cluster numbers from 2 to 10 – see steps 5 and 6 of Fig. 6. The optimal number of clusters was defined by evaluating the performance of multiple indexing criteria (i.e., Calinski-Harabasz, Davies-Bouldin, and Silhouette) to overcome any limitations

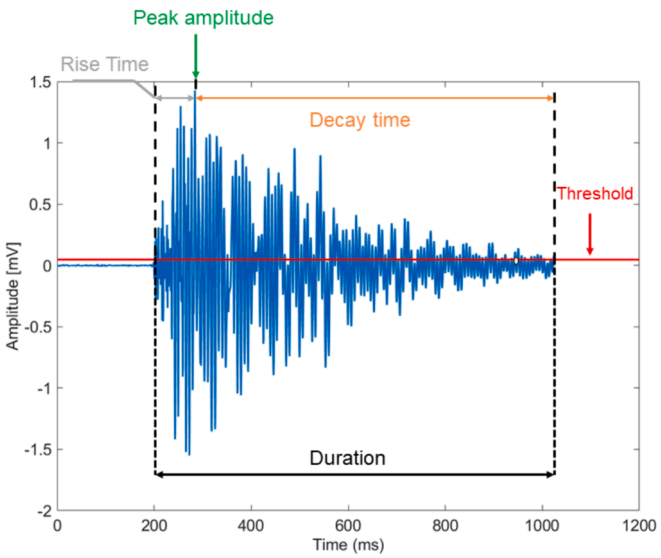

Fig. 3. Representative waveform of the studied composite bonded joints.

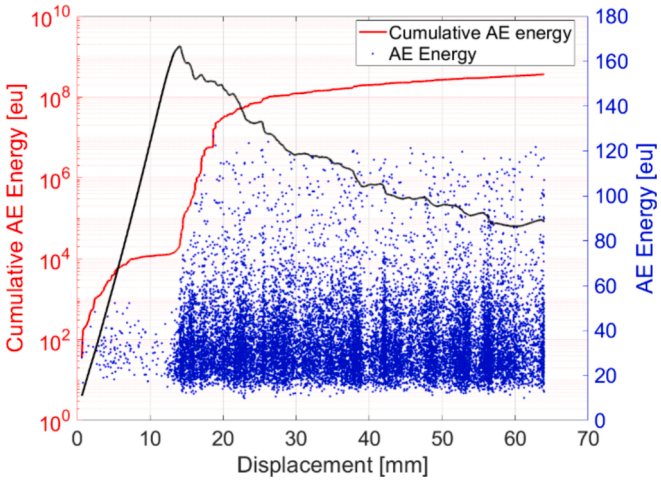

Fig. 4. Acoustic emission energy raw data in function of the load–displacement for AF-0 specimens.

of each criterion, as detailed in [38,52,54].

In general, the performance of the indexing criteria was evaluated by creating a scoring system that attributes points for all the sorted clusters determined by each criterion (best to worst – descending order). Each n^{th} cluster gets the following points: $Cluster_{max} - Cluster_{min} - n$. In which $Cluster_{max}$ represents the number of the best-performing clusters, $Cluster_{min}$ the worst one and n the current number of the cluster. Finally, the points for each n^{th} cluster following each index criterion are determined, and the final optimal cluster number is calculated.

For most specimens, an optimal number of clusters equal to 5 was found – see step 6 in Fig. 6. Therefore, a fixed number of five optimal clusters was defined for each specimen type to facilitate comparing the specimens with different stacking sequences.

4.2. Continuous wavelet transform (CWT)

The complex Morlet wavelet was applied in this work as an additional tool to understand better the relationship between the AE waveform features and the damage mechanisms within the joints, which could not be fully explained by the applied clustering system based on the unsupervised artificial neural network.

Continuous wavelet transform is a self-adaptive time–frequency signal processing method which identifies the transient nature of wave propagation phenomena that time-domain and FFT analysis cannot thoroughly analyse [47,55,56]. The CWT performs a convolution between the original signal and a set of wavelets defined for a specific range of frequencies to extract the time–frequency domain information from the acoustic emission sources [57]. Furthermore, the complex Morlet wavelet is one of the most commonly used mother wavelets for damage identification in composites due to its high localisation in time and frequency achieved by a Gaussian window tapping a complex oscillation over a narrow frequency band, as detailed in [27].

5. AE clustering results and physical interpretation

Table 3 lists the clusters identified in the complete experimental campaign and their corresponding average peak frequency values. Fig. 7 shows the results of the clustering methodology for each specimen type and a representative fracture surface. The plot on the left-hand side shows the typical load–displacement curve and the cumulative energy of each cluster. The plot on the right-hand side shows each acoustic emission source's amplitude versus frequency values divided into different clusters and the average peak frequency of each cluster. It is worth mentioning that, despite the data analysis imposed five clusters for each specimen data, not all specimens presented the same five clusters (energy and peak frequency values). Therefore, 7 clusters were identified in the complete experimental campaign, as shown in Table 3.

As shown in Fig. 7, the most energetic clusters (higher values of cumulative energy – left plots) are clusters *a* and/or *c* for almost all the specimens except for AF-90/0, in which the most energetic cluster is *b* – *see* Fig. 7*d*. It is worth mentioning that, despite the high energy values, clusters *a* and *c* present low values of average peak frequency, about 35 and 130 kHz, respectively. In addition, specimens CFRP (Fig. 7a), AF-90/45 (Fig. 7 e), and AF-90/60 (Fig. 7 f) present a significant number of waveforms grouped in cluster f (average peak frequency larger than 300 kHz). Finally, AF-90/45 specimens (Fig. 7e) are the only ones presenting cluster *g*, with a peak frequency close to cluster *c* (average peak frequency 120 kHz and 130 kHz, respectively). These two adjacent clusters probably result from the five clusters "imposed" by the data processing methodology.

It is worth noticing that each increase in the cumulative energy values of a specific cluster is associated with a drop in the load–displacement curves and, consequently, the initiation and propagation of substantial damage within the joint [24,28,33,58]. This can be seen in Fig. 7 (c), where the first load drop is followed by different cumulative energy curves that present different trends depending on the specimen's load–displacement stage. For example, a high increase in clusters (a) and (c) was observed at the first load drop.

In addition, not all the AE clusters started from the beginning of the test. Looking at the cumulative energy curves, it is possible to see that some clusters began to increase their energy values not at the increase of the load–displacement curve but at the crack propagation stage of the test (after the maximum load), as can be seen for cluster e of CFRP specimen, for example – see Fig. 7 (a).

Ideally, each of these seven clusters will be associated with a specific damage mechanism occurring in the fracture process of the DCB composite bonded joint. However, even though the acoustic emission data was clustered and the literature has an overall comprehension regarding the frequency ranges of matrix cracking and fibre breaking of composites [28,59], insufficient information exists to associate the assessed AE clusters to various fracture mechanisms of the studied composite adhesively bonded joints.

Therefore, labelling the clustered data with the observed fracture mechanisms triggered during the DCB tests for each tailored stacking sequence is crucial. For this, the images from the travelling microscope associated with the load versus displacement curves were used to give physical meaning to the defined clusters. A more detailed analysis of the

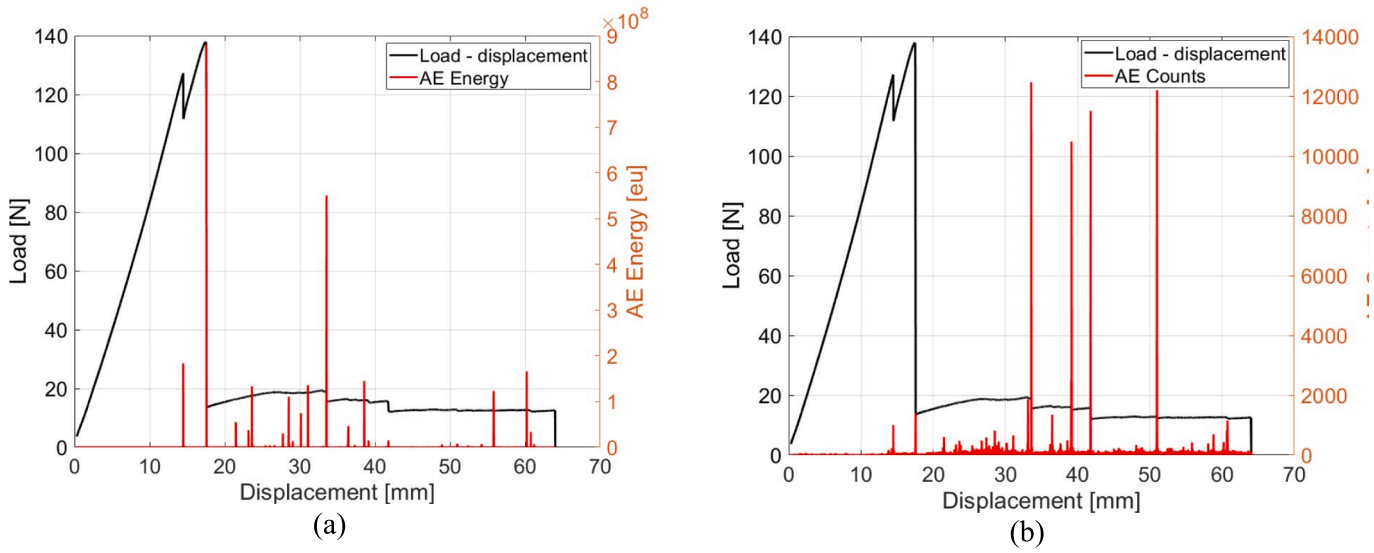

Fig. 5. (a) AE Energy and (b) AE count values related to the load–displacement curve and corresponding fracture surfaces for AF-0/90 specimens.

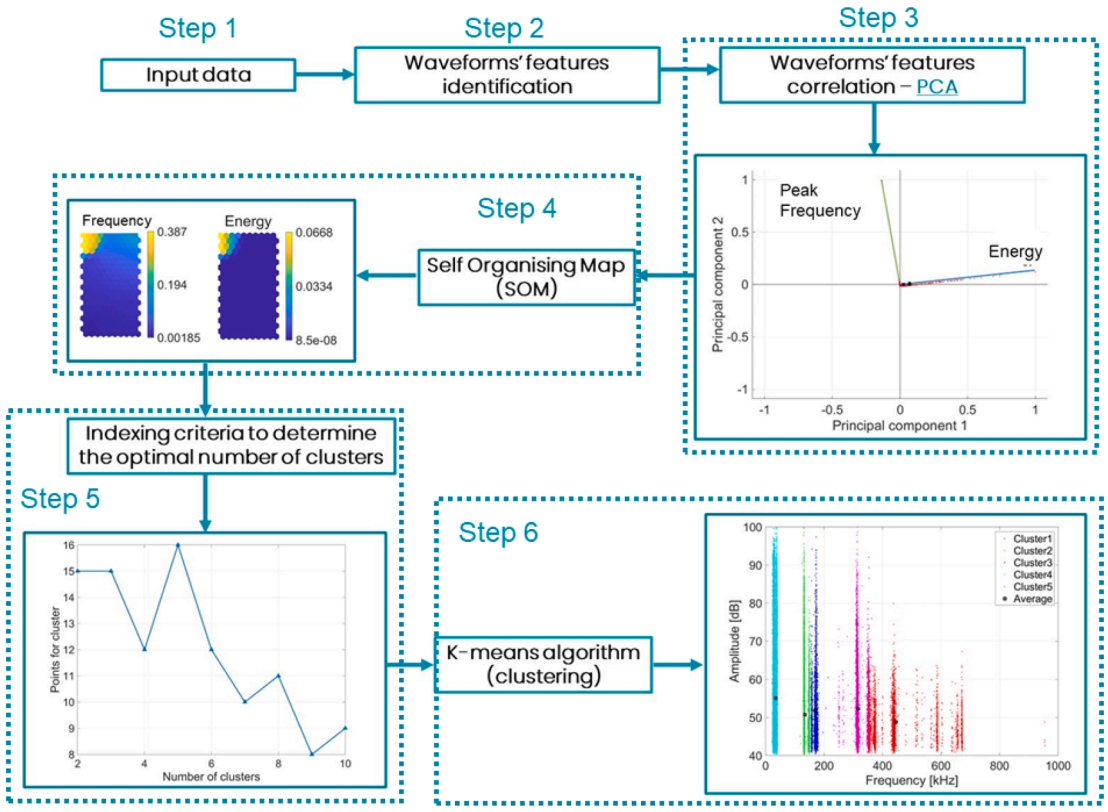

Fig. 6. Scheme of the AE post-processing and clustering methodology.

Table 3
Type of clusters.

Cluster	Colour	Average frequency
a	Light blue	35 kHz
b	Orange	60 kHz
c	Light green	130 kHz
d	Dark blue	170 kHz
e	Pink	255 kHz
f	Red	Higher than 300 kHz
g	Dark green	120 kHz

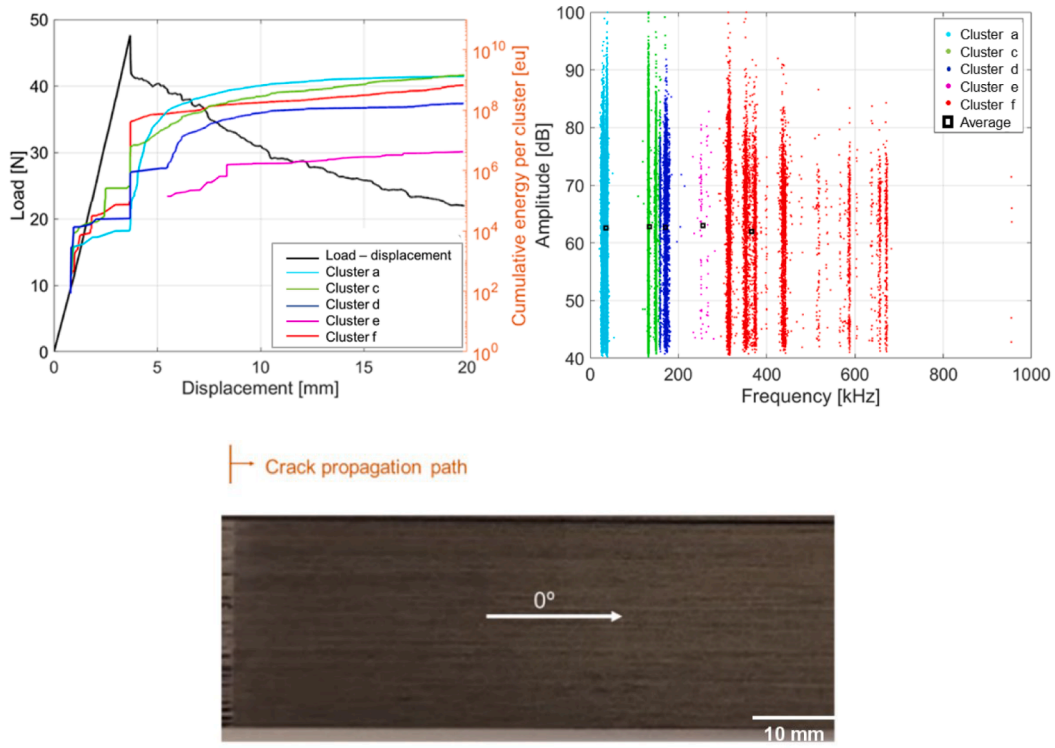

(a) CFRP

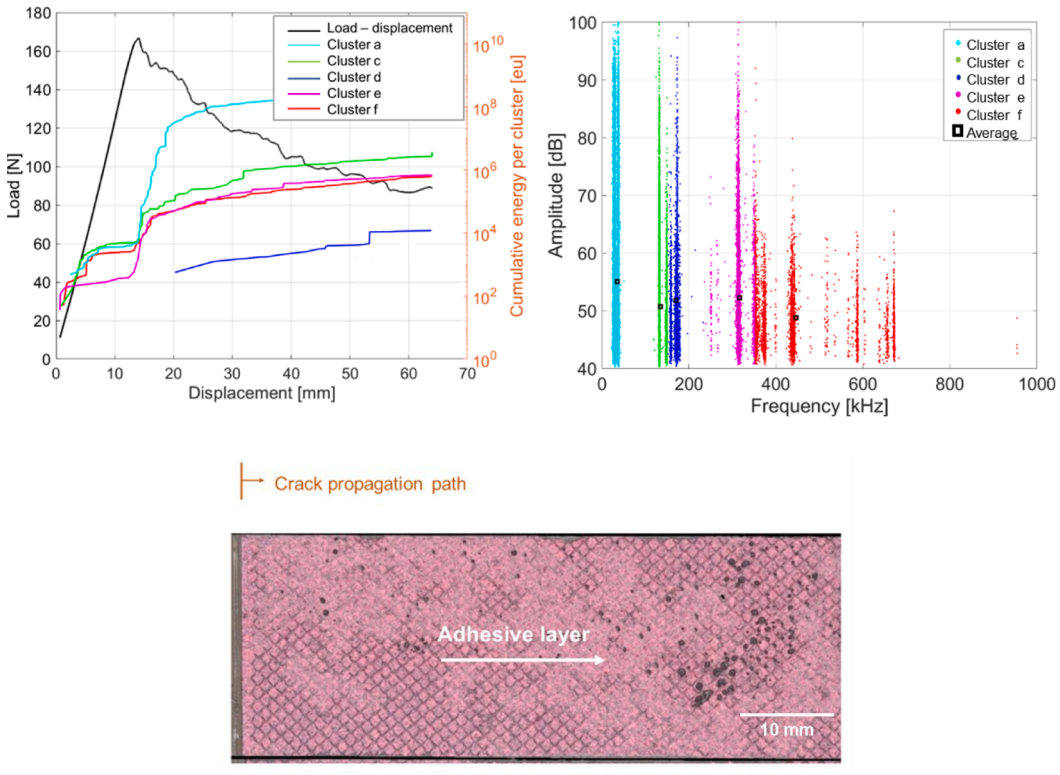

(b) AF-0

Fig. 7. Cumulative energy (left-hand side plots), amplitude versus frequency (right-hand side plots) for each cluster as well as a representative fracture surface of (a) CFRP, (b) AF-0, (c) AF-0/90, (d) AF-90/0, ϵ AF-90/45 and (f) AF-90/60 specimens.

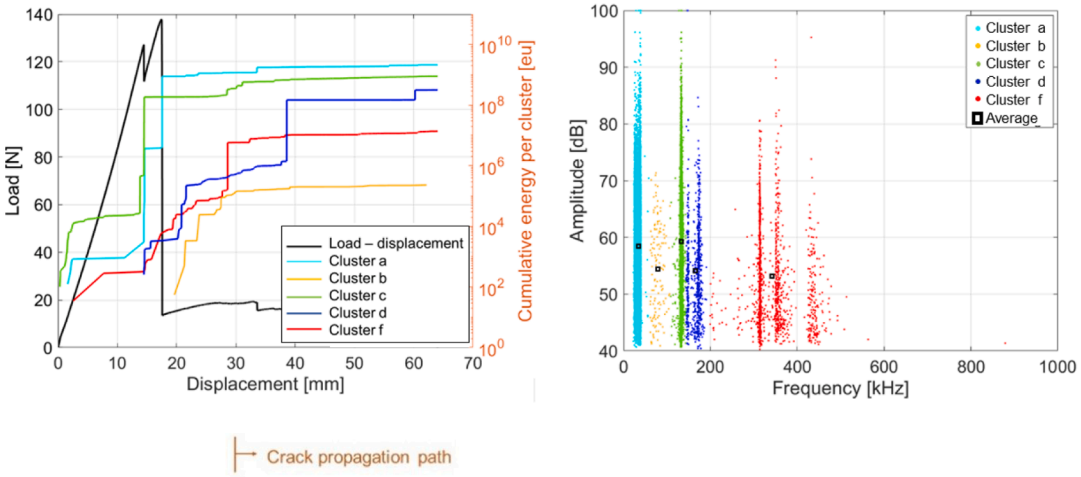

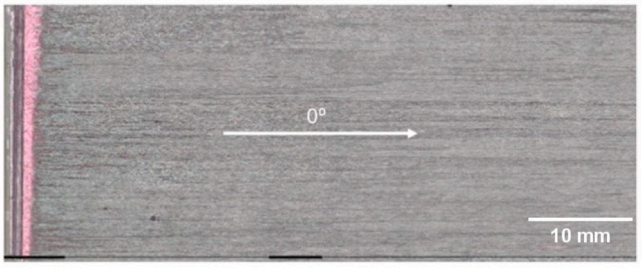

(c) AF-0/90

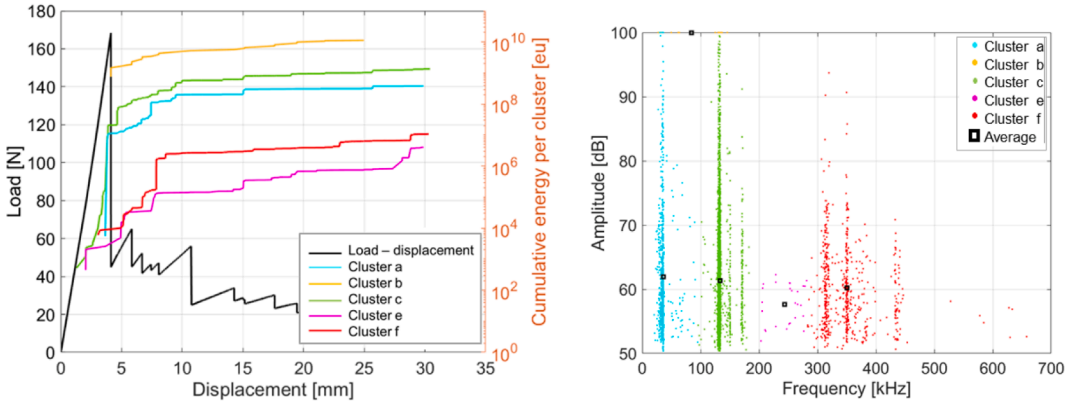

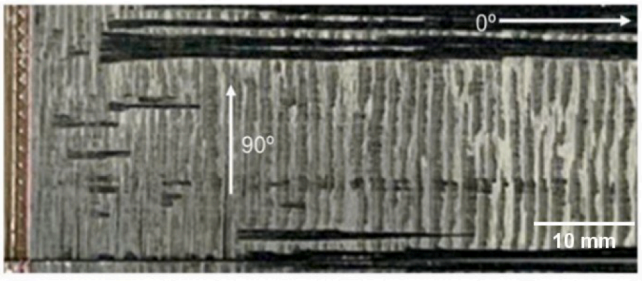

(d) AF-90/0

Fig. 7. (*continued*).

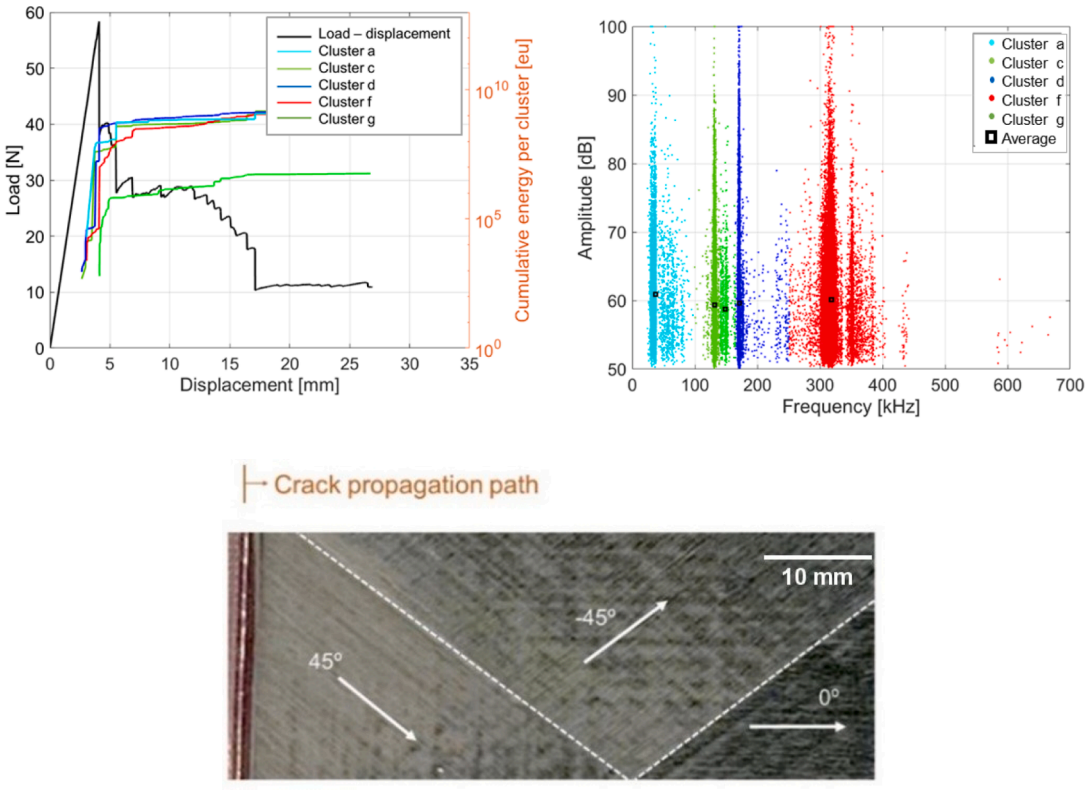

(e) AF-90/45

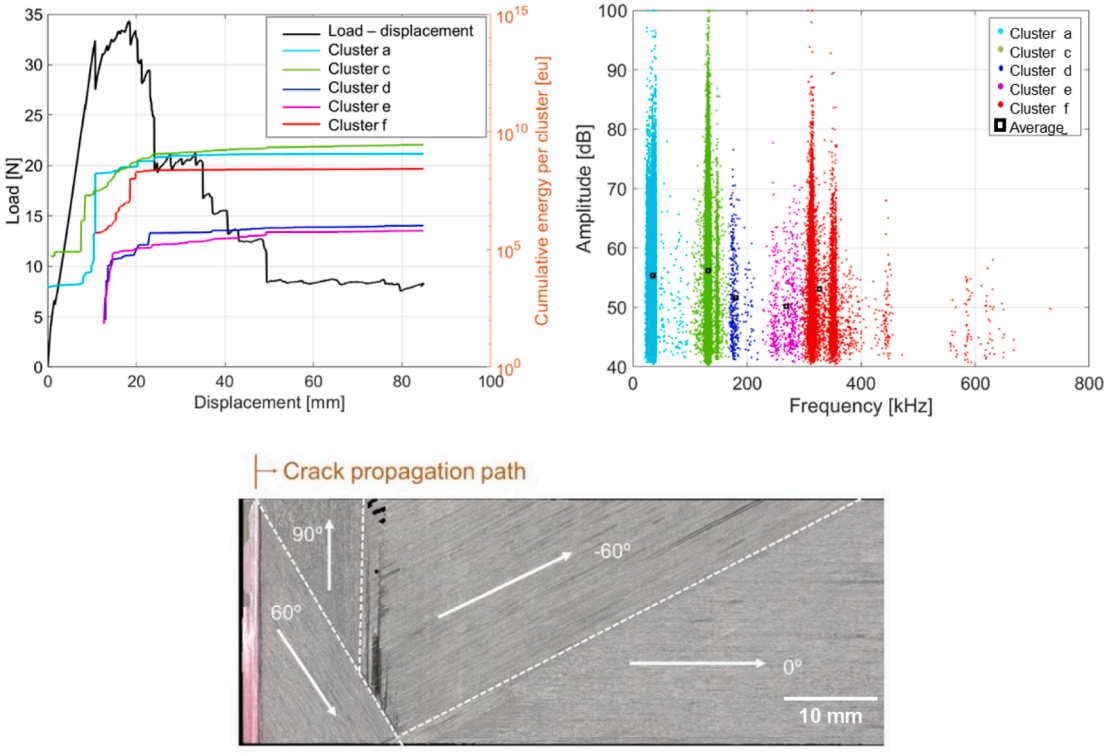

(f) AF-90/60

Fig. 7. (*continued*).

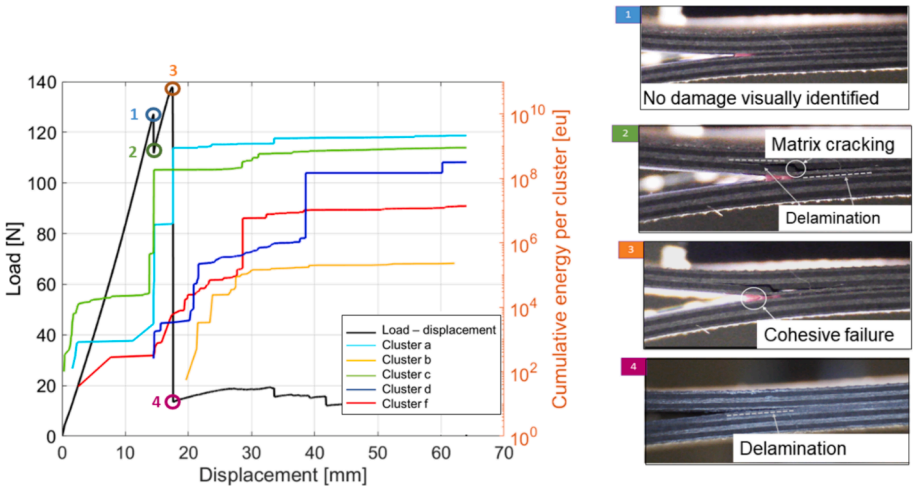

Fig. 8. Relationship between the observed damage mechanisms using the travelling microscope and the load–displacement curve of the AF-0/90 specimen.

different fracture mechanisms triggered by the proposed stacking sequences in the composite joints and their influence on the effective energy release rate onset can be found in [14].

5.1. Attribution of a physical meaning for the AE clusters

Considering the fracture mechanisms described in [14], the following mechanisms are expected to be identified:

- Cohesive failure;
- Delamination (interlaminar crack propagation);
- Fibre breaking;
- Fibre pull-out;
- Matrix cracking;
- Matrix/fibre debonding.

Specimens AF-0/90 and CFRP were selected as representative examples of the methodology used for labelling the AE cluster with the fracture mechanisms. These specimens were selected since they present a clear and direct relationship between the load versus displacement curve and the observed fracture mechanisms and clusters.

5.1.1. AF-0/90 specimen

Fig. 8 shows the representative load versus displacement curve of AF-0/90 with corresponding pictures of the travelling microscope. These specimens present a particular load versus displacement curve with two peak values triggered by two damage mechanisms.

As shown in Fig. 8, no damage could be visually identified at the first peak load (point 1). This was followed by a drop in the load value (point 2) in which a matrix cracking (90/90° ply) and a slight delamination (90/0° interfaces) could be observed. After that, a second load peak (point 3) was identified and correlated to the cohesive failure observed using the travelling microscope. Finally, an abrupt drop in the load–displacement curve was observed due to the final delamination at the 0/90° interface (after point 4).

Paying particular attention to the cumulative energy curves for each cluster makes it possible to observe the following:

- load increase until first peak load (before point 1): clusters *a*, *f* and *c* present AE activity without any considerable change in their trend;
- point 2: a significant increase in the cumulative energy values of clusters *a* and *c* (35 and 130 kHz of average peak frequency, respectively) and the appearance of cluster *d* (170 kHz of average peak frequency);
- point 3: very significant increase in the cumulative energy curve of cluster *a* and a gradual rise in cluster *f* (300 kHz of average peak frequency);
- from point 4 until the end of the test: the appearance and the very significant increase of cluster *b* (60 kHz average peak frequency) and a substantial increase in the cumulative energy of clusters *f* and *d*.

Considering that a significant increase in the cumulative energy curve was observed for clusters *a* and *c* at point 2, they can be associated with the two main damage mechanisms triggered at this instance: matrix cracking in the 90° plies and slight delamination in their vicinity.

At point 3, only cluster *a* had a significant rise in its trend, and at this point, a cohesive failure was observed within the adhesive layer. Hence, this cluster can be associated with the AE sources from the development and final cohesive failure within a polymeric matrix, particularly the adhesive layer.

Delamination, as an interlaminar damage mechanism formed by the micro-damage and matrix cracking that leads to the separation of the composite plies [40,60,61], was observed in the second drop of the load–displacement curve (point 4), where cluster *b* started and had a massive rise. It is worth mentioning that fibre bridging was also noticed during the delamination of the specimens, so fibre–matrix debonding, fibre pull-out and fibre breaking would also be expected.

Therefore, from this specimen and considering that low-frequency clusters are related to matrix cracking and high frequency to fibre-breaking [24,26,41,59,62], the following assumptions could be made:

- cluster *f* (300 kHz to higher frequency values) – fibre breaking. The multiple frequency peaks present in this cluster can be correlated to different kinds of fibre breaking present in the specimen, such as bundle breaking or single fibre breaking [63,64];
- cluster *d* (170 kHz) – probably related to fibre–matrix debonding or fibre pull-out phenomenon due to fibre-bridging within the specimens. Using only the optical microscope camera observation and the clustering method, it was not possible to make the distinction between them;
- cluster *c* (130 kHz) – matrix cracking;
- cluster *b* (60 kHz) – delamination;
- cluster *a* (35 kHz) – looking only at this specimen type and the microscope pictures, this cluster could be defined as the cohesive failure of the adhesive layer. However, this cluster is present in all the other specimens (see Fig. 7) even when no adhesive layer was present, as in the CFRP specimen. Further analysis is needed to label this cluster correctly.

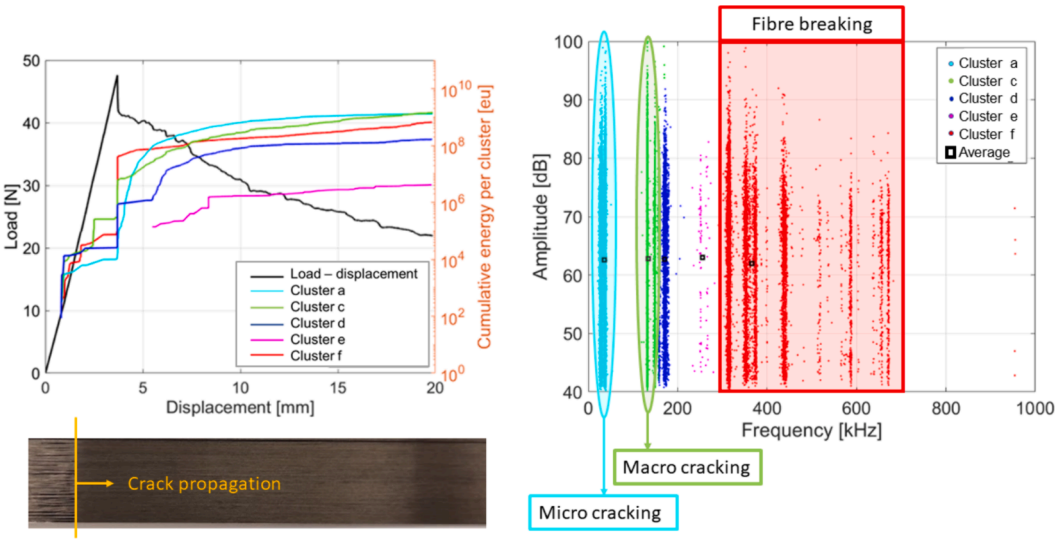

Fig. 9. Clustering of the CFRP specimen and assumed physical meaning.

Since the dark blue cluster *d* and the light blue cluster *a* still lack a clear physical meaning, other specimen types must be used to help label the clusters. The CFRP specimen was chosen since this specimen type did not present an adhesive layer, helping to understand the real meaning of cluster *a*.

5.1.2. CFRP specimen

Fig. 9 shows the clustering of the CFRP specimen and the corresponding physical meaning based on the previous analysis.

As shown in Fig. 9, the CFRP specimen presented cluster *a* (light blue – 35 kHz). Considering that AE sensors can also assess micro-damage fracture mechanisms characterised by very low-frequency values [62], this cluster represents the micro-cracking of the composite matrix.

The green cluster *c* represents the coalescence of these micro-cracks, identified by macro cracking, in the CFRP and AF-0/90 specimens. Interestingly, it was possible to determine the evolution of simultaneous damage mechanisms using the acoustic emission method for the micro-damage development (light blue cluster *a*) and coalescence until the matrix cracking and/or cohesive failure (green cluster *c*). This was also the case for the specimen AF-0 (Fig. 7b), which shows pure cohesive failure: both clusters *a* and *c* are dominant in the crack propagation region, showing the micro cracking ahead of the crack tip with cluster *a* and the coalescence of the micro damage represented by cluster *c* – see Fig. 7 b).

The clusters still to be identified in terms of physical meaning are *d* and *e*. Following the expected fracture mechanisms, a distinction between fibre/matrix debonding and fibre pull-out is still missing. The continuous wavelet transform was used by combining the time and frequency domain of the AE waveforms to provide more information on clusters. The aim was to confirm the physical meaning already attributed to the clusters *a*, *b*, *c* and *f* considering the cumulative energy approach and to identify the fracture mechanisms yet to be identified with the remaining clusters (*d* and *e*).

Fig. 10 shows the Morlet wavelet transform's spectrogram in the frequency and time function of the CFRP (bottom image; the colour scale represents the waveform's amplitude). The representative waveform and its frequency profile are also shown for each cluster (top side of the image – left and right sides, respectively), where P1(f) represents the single-sided amplitude spectrum from the FFT of the waveform.

Fig. 10 (a) and (b) show representative waveforms of clusters *a* (35 kHz average peak frequency and *c* (130 kHz average peak frequency) associated previously with micro and macro damage of the polymeric matrix, respectively. Cluster *a* shows a spectrogram with a maximum peak frequency of 35 kHz and high amplitude values for a longer duration (300 to 800 ms). Cluster *c* shows a spectrogram with a maximum peak frequency of 130 kHz and a second peak frequency of 35 kHz. The duration of the AE hit of 130 kHz is smaller when compared with the one with a maximum peak frequency of 35 kHz; see the total time where the high amplitude values are present in the waveform's spectrogram Fig. 10b. This cluster c was associated with the matrix's macro-damage (crack propagation); however, there is a representative part of its amplitude in the small frequency values as well, showing the presence of AE micro-damage signals together with the macro-damage development.

Fig. 10 (c) and (d) show the representative waveforms of clusters dark blue *d* (170 kHz) and pink *e* (255 kHz), respectively. The spectrogram of both clusters presents high amplitude values in the waveform in a short time. Moreover, multiple peak frequencies were observed, including the ones associated with micro and macro damage of the matrix and fibre breakage. In the previous section, it was impossible to distinguish them regarding the fracture mechanisms they would represent, such as fibre/matrix debonding or fibre/matrix pull-out.

From the Morlet CWT spectrogram of these specific clusters, it is possible to notice a difference in the frequency level where the waveforms have the highest amplitude values. The dark blue cluster *d* presents the highest amplitude values around 170 kHz at 200 ms. The pink cluster *e* instead presents the highest amplitude value around 400 kHz even though its maximum peak frequency is at 255 kHz (see Fig. 10e), indicating a significative influence of the frequency signature related to fibre breaking also in this cluster. Accordingly, since the fibre–matrix debonding is a mechanism formed by the micro damage formation and final crack propagation in the fibre/matrix interface and the fibre pull-out is formed by the co-occurrence of fibre-breaking in combination with the matrix cracking in a way that the fibre can be pulled from the matrix, it is coherent to expect also a combination of different frequency signatures in their representative waveforms [40,66,67]. Therefore, the pink cluster *e* can be associated with the damage mechanism of fibre pull-out, and the dark blue cluster *d* can be labelled as fibre/matrix

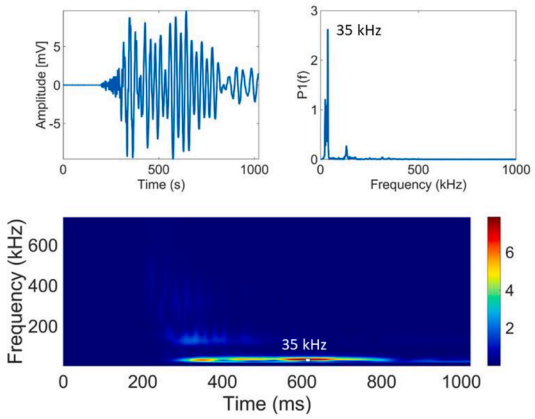

(a) Light blue cluster *a* – 35 kHz of peak frequency

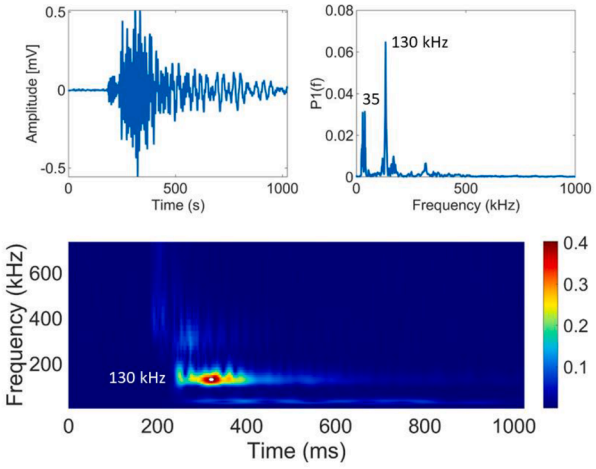

(b) Green cluster *c* – 130 kHz of peak frequency

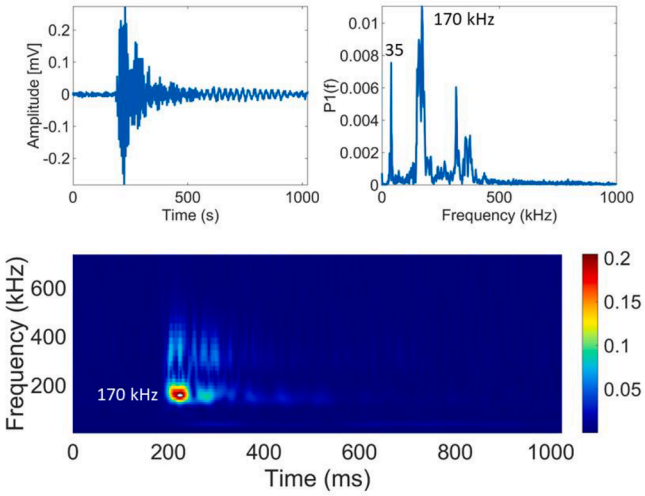

(c) Dark blue *d* – 170 kHz of peak frequency

Fig. 10. Morlet continuous wavelet transform of CFRP specimen for (a) light blue, (b) green, (c) dark blue, (d) pink and (e) red clusters (the colour scale represents the waveform's amplitude). (For interpretation of the references to colour in this figure legend, the reader is referred to the web version of this article.)

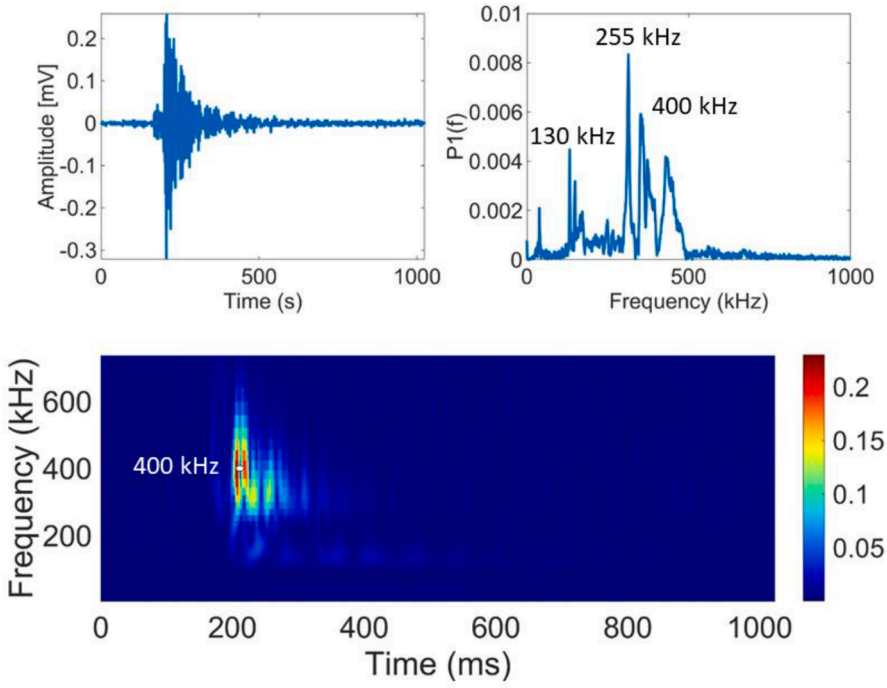

(d) Pink cluster *e* – 255 kHz of peak frequency

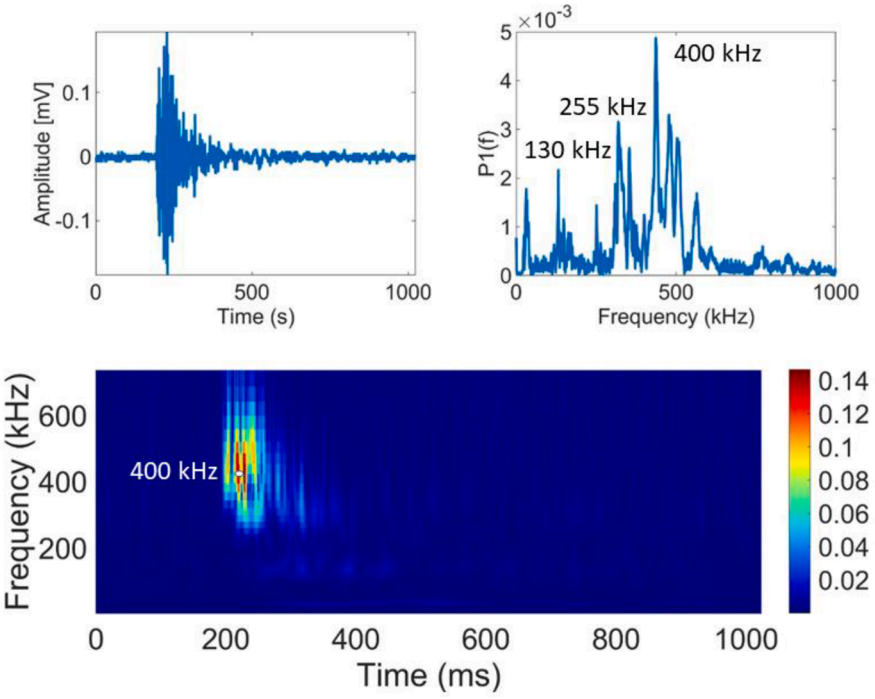

(e) Red cluster *f* – 300 kHz to higher values of peak frequency

Fig. 10. (*continued*).

Table 4
Average frequency values for each type of damage mechanism observed during the quasi-static DCB tests.

Damage mechanisms	Micro-cracking	Delamination	Matrix cracking	Fibre-matrix debonding	Fibre pull-out	Fibre failure
Cluster	*a*	*b*	*c*	*d*	*e*	*f*
Associated colour	Light blue	Orange	Green	Dark blue	Pink	Red
Peak frequency (kHz)	35	60	130	170	255	300 to higher values
Frequency – highest amplitude value (CWT)	35	60	130	170	400	400
CFRP	✓	✗	✓	✓	✓	✓
AF-0	✓	✗	✓	✓	✓	✓
AF-0/90	✓	✓	✓	✓	✓	✓
AF-90/0	✓	✓	✓	✓	✓	✓
AF-90/45	✓	✓	✓	✓	✓	✓
AF-90/60	✓	✓	✓	✓	✓	✓

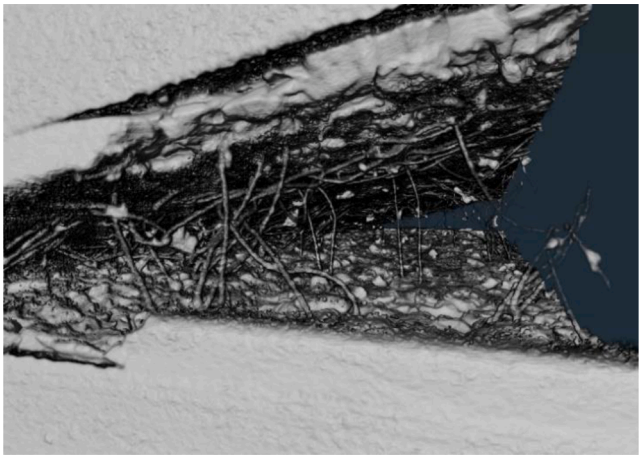

Fig. 11. Micro CT image of AF-0 specimen at the beginning of the specimen next to the crack tip.

debonding. The summary of the types of damage mechanisms associated with each cluster is detailed in Table 4, as well as their presence or absence in the different types of tested specimens. As seen in Table 4, the frequency values with the highest amplitude values are not always the highest peak frequency values. This phenomenon can give an insight into the simultaneous occurrence of different damage mechanisms within the same waveform (i.e. matrix cracking and fibre breakage in the fibre pull-out signature) and be used as a crucial factor for understanding the clusters' physical meaning and the complexity of the damage evolution within the joints.

The specimen AF-0 presented a complete cohesive failure. However, Table 4 showed AE clusters of this specimen related to micro-cracking, macro-cracking, fibre/matrix debonding, fibre pull-out and fibre breakage. To explain the existence of these clusters in these specimens, Fig. 11 shows a Micro CT image of this specimen at the crack front – at the beginning of the specimen next to the crack tip.

As observed, the cohesive crack propagation is not only characterised by polymeric/matrix cracking. Instead, a more complex phenomenon is observed. Due to a bridging mechanism triggered by the nylon carrier embedded within the adhesive layer, in the crack propagation process, the nylon fibres debonded from the adhesive material, stretched, held the substrate's arms and finally broke. A fibre-bridging mechanism was hence triggered, so other mechanisms such as fibre–matrix debonding, fibre pull-out and finally, fibre breakage were recorded. Here, the fibre is the nylon fibres of the adhesive carrier [44,68].

Regarding specimen AF-90/45, it is essential to mention that cluster *g* (dark green – 120 kHz) does not present a clear difference from the light green cluster (130 kHz) being integrated at the same cluster and hence associated with matrix cracking.

The general outcomes and limitations of the clustering and physical meaning associations are discussed in the next section.

5.2. Outcomes and limitations of the methodology

The proposed AE clustering methodology, based on an unsupervised artificial neural network, was crucial for a better understanding of when and which damage mechanisms are triggered within the composite adhesively bonded joints. The peak frequency significantly impacts the clustering of AE data, creating datasets with a narrow average frequency, except for the cluster for the fibre breakage (frequency values higher than 300 kHz).

It was noticed that the acoustic emission method is highly sensitive to the micro-damage formation and their final coalescence (crack propagation) – clusters light blue *a* and green *c* with more hits and higher cumulative energy values in most of the tested specimens. Additionally, it is possible to identify the regions in the material where micro-damage is being formed and, consequently, higher energy is being stored within the material; meanwhile, different new micro-damage paths are being created, possibly increasing the joint's fracture toughness and delaying crack propagation. As could be observed on the second peak of the load versus displacement curve of specimen AF-0/90, a massive increase in the cumulative energy of cluster *a* (light blue) was observed.

By the Morlet CWT analysis, it was possible to verify that damage mechanisms such as delamination and fibre pull-out are complex and formed by a combination or simultaneous occurrence of, for example, macro cracking and fibre breakage.

Surprisingly, the acoustic emission cluster associated with the delamination phenomenon was not present in the CFRP. The delamination cluster seems only be identified as a single cluster (with a maximum peak frequency of 60 kHz) under mode I loading when the preferential path for the crack propagation changes and delamination occurs, as the case for the other specimens' types AF0/90, AF90/0, AF90/45 and AF90/60. Since the CFRP specimen's crack propagation was at the same plane where the Teflon insert was embedded, the main damage mechanisms identified were micro-damage, matrix cracking and those related to fibre bridging, i.e., fibre pull-out and fibre breaking. In the literature, delamination is defined as an interlaminar damage mechanism formed by the micro-damage and matrix cracking that leads to the separation of the composite plies, so these mechanisms were actually identified in the specimens CFRP [40,64,65].

Furthermore, for the CFRP specimen, a high number of hits related to fibre breaking was identified compared to the other types of specimens, indicating a higher presence of fibre bridging during the tests.

It was observed that a fixed number of clusters for all the specimens is not always the best clustering solution. It facilitates the comparison and overview analyses of the damage mechanisms but can be unrealistic. The filtering regarding the number of counts for eliminating background noise seemed sufficient, but some waveforms related to noise or friction may still be present in the clusters.

Finally, the most outstanding result is the observance of the co-occurrence of different damage mechanisms represented as the multiple frequency peaks within the AE waveforms. Each frequency peak is associated with specific amplitude values that do not always have higher values for the highest frequency peak. The high amplitude values in the CWT spectrogram can indicate the most significative frequency peak for each waveform, providing relevant knowledge for understanding complex non-visible damage mechanisms and their evolution during the DCB tests.

For future developments, the labels proposed here in this work can be further used in supervised artificial neural networks and other loading conditions where the visual evaluation of the fracture mechanisms is limited, as in mode II or III and mixed mode loading conditions, both in quasi-static and fatigue loading. With the methodology and insight developed in this study, one could identify the damage mechanisms in composite adhesively bonded joints and exploit if the different loading conditions and fracture mechanisms can generate new AE clusters.

It is worth noting that real-time monitoring of bonded structures using the acoustic emission method can pose significant challenges, especially when it comes to dealing with higher background noise and exposure to environmental conditions. Moreover, scaling up the technique for larger structures adds to the complexity of identifying damage mechanisms and understanding the joint's fracture behaviour. Therefore, further research should consider the SHM of in-service bonded joints.

6. Conclusions

The AE method's feasibility was studied to identify and better understand the initiation and propagation of different fracture mechanisms within composite adhesively bonded joints with tailored stacking sequences under quasi-static mode I loading conditions. The AE waveforms were clustered and classified using an unsupervised artificial neural network and Morlet continuous wavelet transform. The following conclusions can be defined:

- Non-visible damage mechanisms triggered within the joints could be identified using the acoustic emission method, proving to be an additional tool for understanding the toughening phenomena of the joints;
- the proposed clustering methodology combining the k-means and self-organising map algorithms, visual evaluation of the fracture surfaces and continuous wavelet transform gave a robust clustering of the AE hits, allowing physical meaning for the AE clusters that can be used in future works considering different loading conditions and supervised algorithms;
- acoustic emission frequency signatures of the cohesive failure from adhesively bonded composite joints (using epoxy adhesive film) are proven to be consistent with those correlated to matrix cracking in the structures without bondlines;
- the co-occurrence of different damage phenomena could be verified and better understood by applying representative CWT spectrogram analysis. In particular, damage mechanisms such as delamination, fibre pull-out and fibre/matrix debonding present significative amplitude values in different frequency ranges;
- the proposed AE clustering system based on the peak frequency and energy is a promising method for in-service damage monitoring of composite adhesively bonded components even when multi-damage mechanisms co-occur, paving a robust path toward accurate diagnoses.

CRediT authorship contribution statement

R.A.A. Lima: Writing – original draft, Visualization, Validation, Methodology, Formal analysis, Data curation. **R. Tao:** Writing – original draft, Visualization, Validation, Resources, Formal analysis, Data curation. **A. Bernasconi:** Writing – review & editing, Supervision, Methodology, Funding acquisition, Conceptualization. **M. Carboni:** Writing – review & editing, Supervision, Methodology, Funding acquisition, Conceptualization. **S. Teixeira de Freitas:** Writing – review & editing, Validation, Supervision, Methodology, Investigation, Funding acquisition, Conceptualization.

Declaration of competing interest

The authors declare that they have no known competing financial interests or personal relationships that could have appeared to influence the work reported in this paper.

Data availability

The Data is available on the DOI:10.4121/21f78a36-d579-4ee8-a3cc-7954e0581da6

Acknowledgements

This article is based upon work from COST Action CA18120 (CERTBOND - https://certbond.eu/), supported by COST (European Cooperation in Science and Technology).

The authors would like to acknowledge Davide Biagini and Morteza Moradi from TU Delft for all the insightful discussions about data post-processing possibilities for the acoustic emission data.

The authors acknowledge Fundação para a Ciência e a Tecnologia (FCT) for its financial support via the project LAETA Base Funding (DOI: 10.54499/UIDB/50022/2020)

Appendix

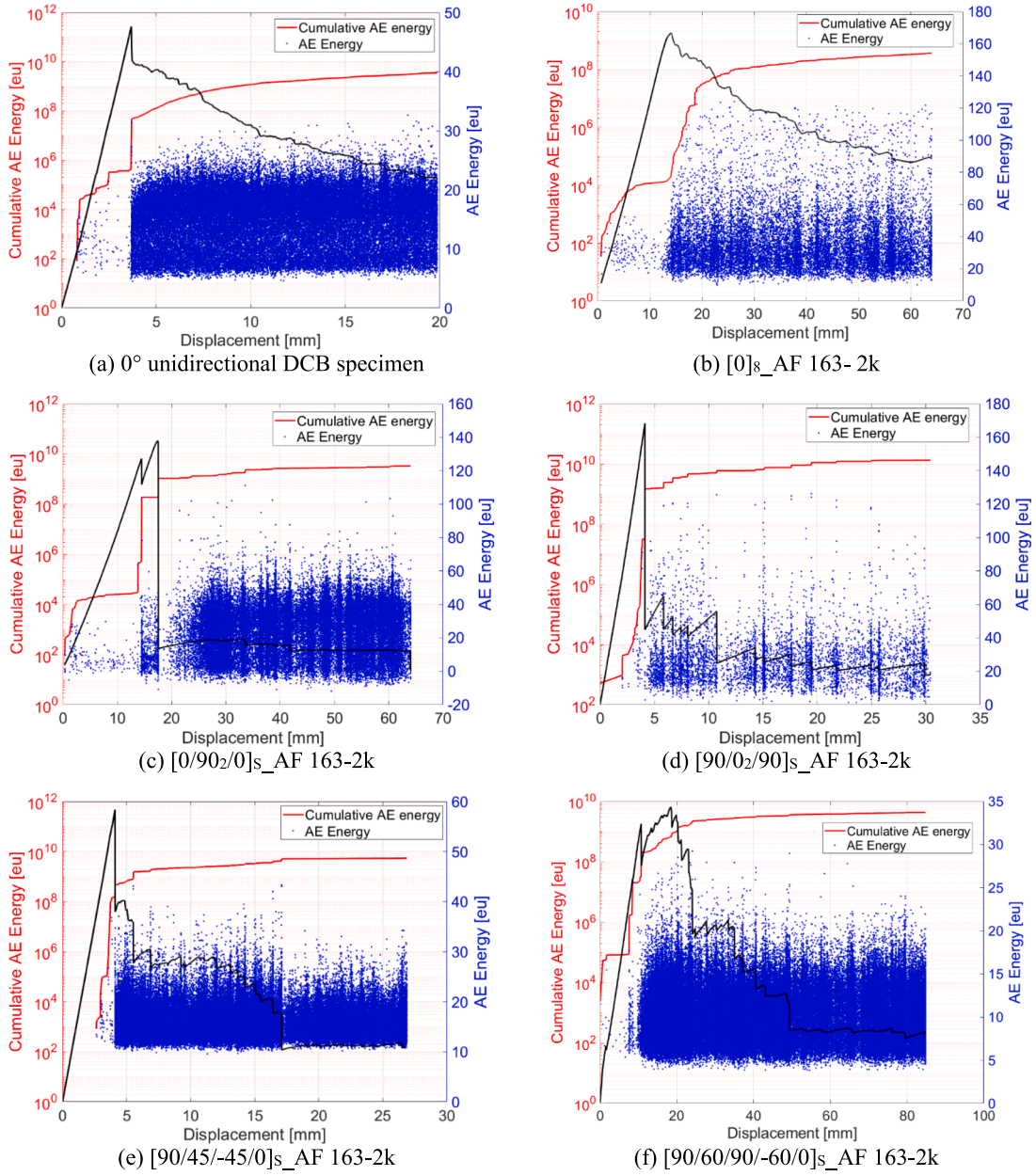

(a) 0° unidirectional DCB specimen

(b) [0]8_AF 163- 2k

(c) [0/902/0]S_AF 163-2k

(d) [90/02/90]S_AF 163-2k

(e) [90/45/-45/0]S_AF 163-2k

(f) [90/60/90/-60/0]S_AF 163-2k

Fig. A.1. [0]8_AF 163–2 k, (c) [0/902/0]S_AF 163–2 k, (d) [90/02/90]S_AF 163–2 k, (e) [90/45/-45/0]S_AF 163–2 k and (f) [90/60/90/-60/0]S_AF 163–2 k specimens.

Appendix B

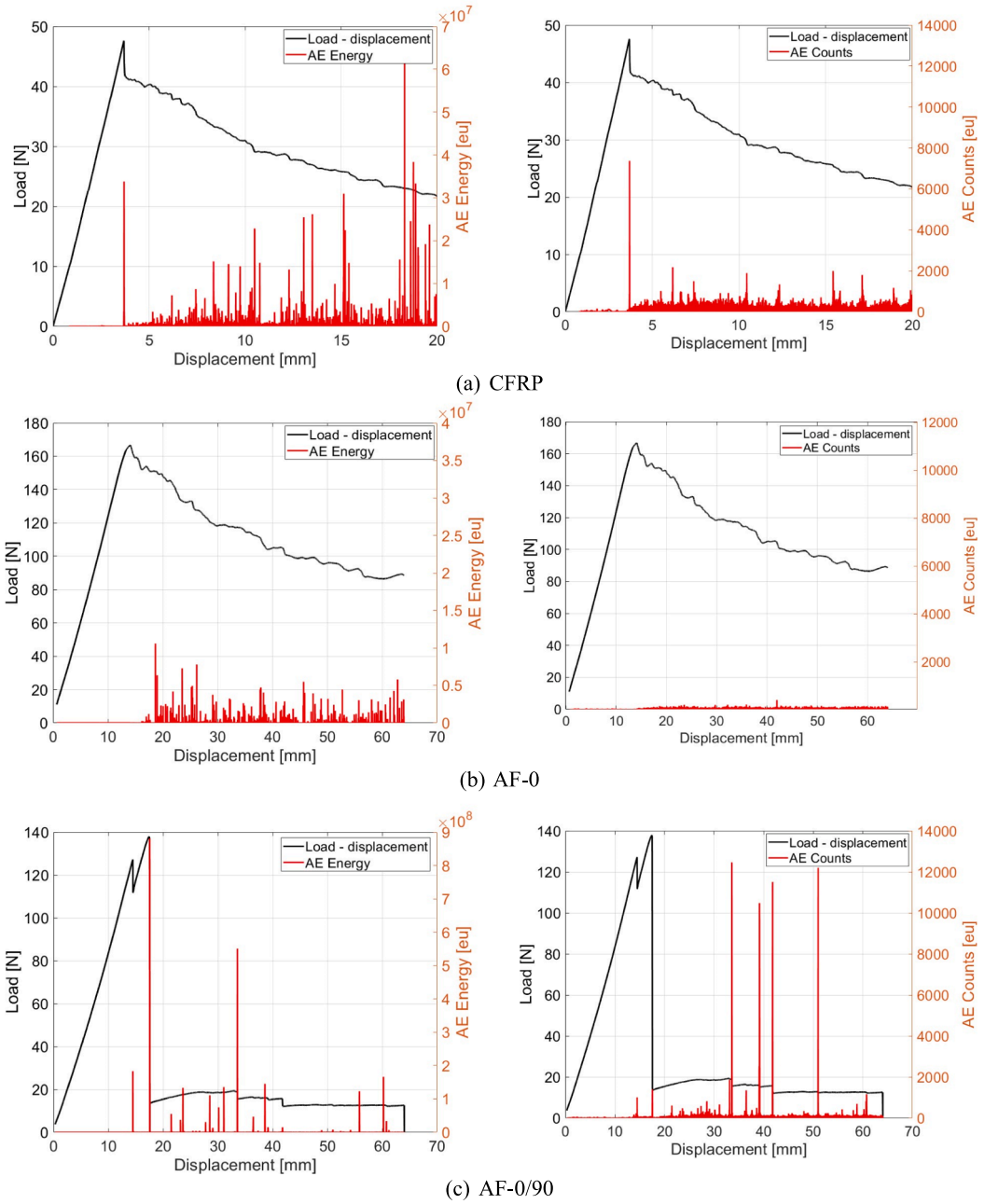

Fig. A.2. Acoustic emission energy raw data and counts related to the load–displacement curve for (a) 0° unidirectional DCB, (b) [0]8_AF 163–2 k, (c) [0/902/0] S_AF 163–2 k, (d) [90/02/90]S_AF 163–2 k, (e) [90/45/-45/0]S_AF 163–2 k and (f) [90/60/90/-60/0]S_AF 163–2 k specimens.

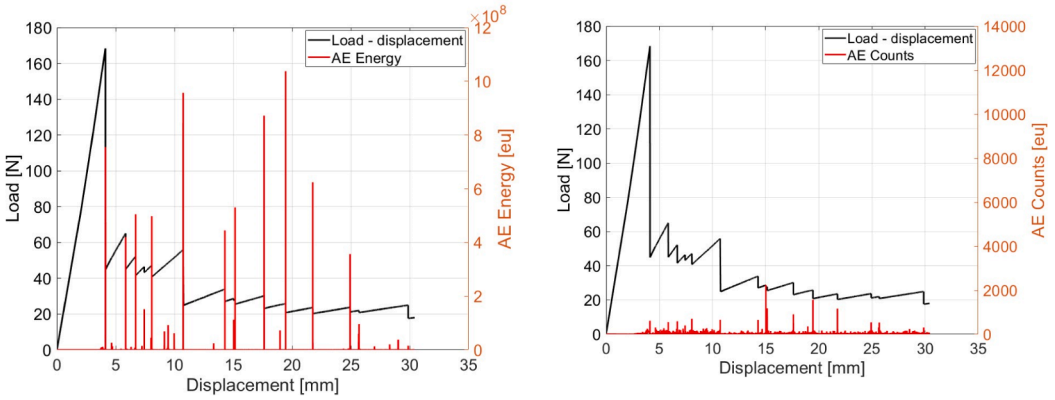

(d) AF-90/0

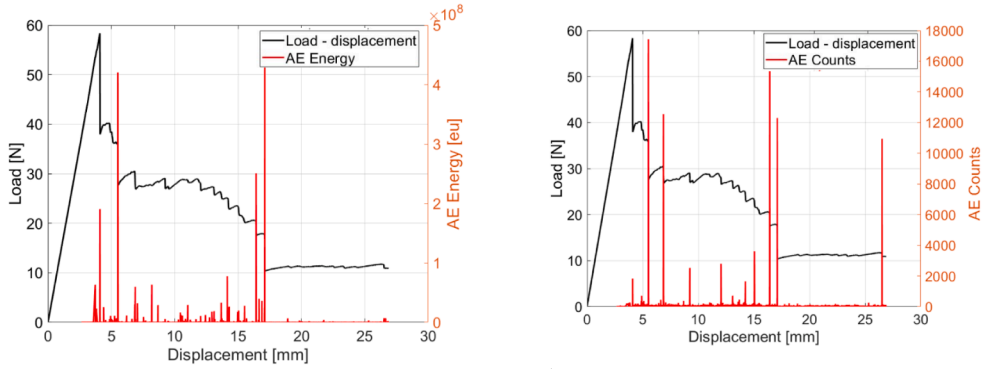

(e) AF-90/45

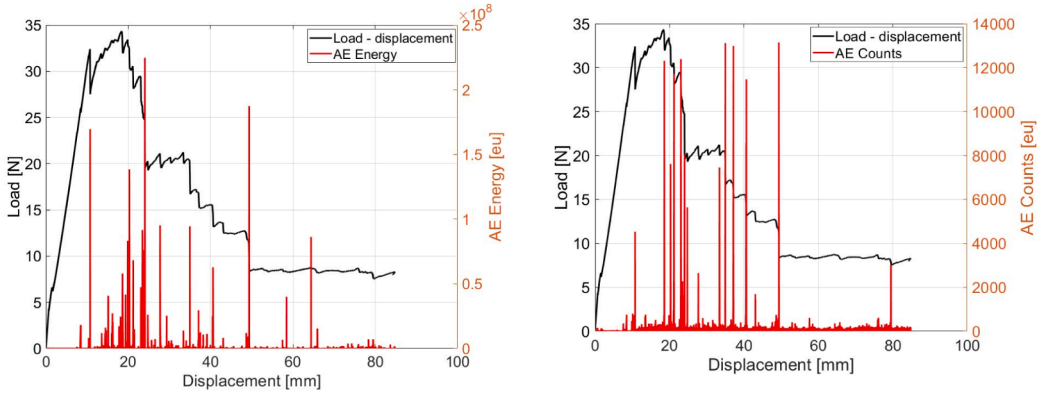

(f) AF-90/60

Fig. A.2. (*continued*).

References

[1] M. Frascio, E. A. D. S. Marques, R. J. C. Carbas, L. F. M. da Silva, M. Monti, and M. Avalle, "Review of Tailoring Methods for Joints with Additively Manufactured Adherends and Adhesives", *Materials*, vol. 13, no. 18, 2020, doi: 10.3390/ma13183949.

[2] A.C. Marques, A. Mocanu, N.Z. Tomić, S. Balos, E. Stammen, A. Lundevall, S. T. Abrahami, R. Günther, J.M.M. de Kok, S. Teixeira de Freitas, Review on adhesives and surface treatments for structural applications: Recent developments on sustainability and implementation for metal and composite substrates, Materials 13 (24) (2020) 1–43, https://doi.org/10.3390/ma13245590.

[3] M.V. Fernández, M.F.S.F. De Moura, L.F.M. Da Silva, A.T. Marques, Composite bonded joints under mode I fatigue loading, Int J Adhes Adhes 31 (5) (2011) 280–285, https://doi.org/10.1016/j.ijadhadh.2010.10.003.

[4] M. Costa, G. Viana, L.F.M. da Silva, R.D.S.G. Campilho, Environmental effect on the fatigue degradation of adhesive joints: A review, J Adhesion 93 (1–2) (2017) 127–146, https://doi.org/10.1080/00218464.2016.1179117.

[5] C. Jeenjitkaew, F.J. Guild, The analysis of kissing bonds in adhesive joints, Int J Adhes Adhes 75 (Jun. 2017) 101–107, https://doi.org/10.1016/j.ijadhadh.2017.02.019.

[6] M.D. Banea, L.F.M. Da Silva, Adhesively bonded joints in composite materials: An overview, Proc. Inst. Mech. Eng. Pt. L J. Mater. Des. Appl. 223 (1) (2009) 1–18, https://doi.org/10.1243/14644207JMDA219.

[7] J.J.M. Machado, E.A.S. Marques, L.F.M. da Silva, Adhesives and adhesive joints under impact loadings: An overview, J Adhesion 94 (6) (2018) 421–452, https://doi.org/10.1080/00218464.2017.1282349.

[8] A. Preisler, Z. Sadeghi, and K.-U. Schröder, "Monitoring of Fatigue Damages in Adhesively Bonded Joints," *Proceedings of the 6th ECCOMAS Thematic Conference on the Mechanical Response of Composites*, no. September, 2017.

[9] J.A.B.P. Neto, R.D.S.G. Campilho, L.F.M. Da Silva, Parametric study of adhesive joints with composites, Int J Adhes Adhes 37 (2012) 96–101, https://doi.org/10.1016/j.ijadhadh.2012.01.019.

[10] K. Maloney, N. Fleck, Toughening strategies in adhesive joints, Int J Solids Struct 158 (2019) 66–75, https://doi.org/10.1016/j.ijsolstr.2018.08.028.

[11] M.D. Banea, L.F.M. Da Silva, R.D.S.G. Campilho, C. Sato, Smart adhesive joints: An overview of recent developments, J Adhesion 90 (1) (2014) 16–40, https://doi.org/10.1080/00218464.2013.785916.

[12] G. Jeevi, S. Kumar Nayak, M. Abdul Kader, Review on adhesive joints and their application in hybrid composite structures, J Adhes Sci Technol 33 (2019) 1497–1520, https://doi.org/10.1080/01694243.2018.1543528.

[13] D. Quan, J.L. Urdániz, C. Rouge, A. Ivanković, The enhancement of adhesively-bonded aerospace-grade composite joints using steel fibres, Compos Struct 198 (Aug. 2018) 11–18, https://doi.org/10.1016/J.COMPSTRUCT.2018.04.071.

[14] R.A.A. Lima, R. Tao, A. Bernasconi, M. Carboni, N. Carrere, S. Teixeira de Freitas, Uncovering the toughening mechanisms of bonded joints through tailored CFRP layup, Compos B Eng 263 (Aug. 2023), https://doi.org/10.1016/j.compositesb.2023.110853.

[15] S. Daynes, P.M. Weaver, Stiffness tailoring using prestress in adaptive composite structures, Compos Struct 106 (2013) 282–287, https://doi.org/10.1016/j.compstruct.2013.05.059.

[16] R.D. Adams, P. Cawley, A review of defect types and nondestructive testing techniques for composites and bonded joints, NDT Int. 21 (4) (Aug. 1988) 208–222, https://doi.org/10.1016/0308-9126(88)90333-1.

[17] N. Eleftheroglou, D. Zarouchas, R. Alderliesten, R. Benedictus, and T. Loutas, "Prognostics of composite structures utilising structural health monitoring data fusion," *9th European Workshop on Structural Health Monitoring, EWSHM 2018*, no. July, 2018.

[18] C.R. Farrar, K. Worden, An introduction to structural health monitoring, Phil. Trans. r. Soc. A 365 (1851) (2007) 303–315, https://doi.org/10.1098/rsta.2006.1928.

[19] M.G.R. Sause, In Situ Monitoring of Fiber-Reinforced Composites, Ssmaterials 242 (2016) 633, https://doi.org/10.1007/978-3-319-30954-5.

[20] V. Giurgiutiu, A. Zagrai, J.J. Bao, Piezoelectric wafer embedded active sensors for aging aircraft structural health monitoring, Struct Health Monit 1 (1) (2002) 41–61, https://doi.org/10.1177/147592170200100104.

[21] P. Manco, M. Caterino, R. Macchiaroli, M. Rinaldi, and M. Fera, "Aircraft Maintenance: Structural Health Monitoring Influence on Costs and Practices," *Macromol Symp*, vol. 396, no. 1, 2021, doi: 10.1002/masy.202000302.

[22] S. Sulejmani, C. *Sonnenfeld, T. Geernaert, G. Luyckx, P. Mergo, W. Urbanczyk, K. Chah, H. Thienpont, and F. Berghmans*, "Disbond monitoring in adhesive joints using shear stress optical fiber sensors," *Smart Mater Struct*, vol. 23, no. 7, 2014, doi: 10.1088/0964-1726/23/7/075006.

[23] C. Kralovec, M. Schagerl, Review of structural health monitoring methods regarding a multi-sensor approach for damage assessment of metal and composite structures, Sensors (switzerland) 20 (3) (2020) 1–25, https://doi.org/10.3390/s20030826.

[24] M. Saeedifar, D. Zarouchas, Damage characterisation of laminated composites using acoustic emission: A review, Compos B Eng vol. 195, no. January (2020) 108039, https://doi.org/10.1016/j.compositesb.2020.108039.

[25] R. de Oliveira, A.T. Marques, Health monitoring of FRP using acoustic emission and artificial neural networks, Comput Struct 86 (3–5) (Feb. 2008) 367–373, https://doi.org/10.1016/J.COMPSTRUC.2007.02.015.

[26] M. Saeedifar, M.A. Najafabadi, D. Zarouchas, H.H. Toudeshky, M. Jalalvand, Barely visible impact damage assessment in laminated composites using acoustic emission, Compos B Eng 152 (June) (2018) 180–192, https://doi.org/10.1016/j.compositesb.2018.07.016.

[27] C. Muir*, B. Swaminathan, A. S. Almansour, K. Sevener, C. Smith, M. Presby, J. D. Kiser, T. M. Pollock, and S. Daly*, "Damage mechanism identification in composites via machine learning and acoustic emission," Npj *Comput Mater*, vol. 7, no. 1. 2021. doi: 10.1038/s41524-021-00565-x.

[28] T. Bohmann, M. Schlamp, I. Ehrlich, Acoustic emission of material damages in glass fibre-reinforced plastics, Compos B Eng 155 (April) (2018) 444–451, https://doi.org/10.1016/j.compositesb.2018.09.018.

[29] E. Maillet, C. Baker, G.N. Morscher, V.V. Pujar, J.R. Lemanski, Feasibility and limitations of damage identification in composite materials using acoustic emission, Compos Part A Appl Sci Manuf 75 (2015) 77–83, https://doi.org/10.1016/j.compositesa.2015.05.003.

[30] A. Crawford, M.G. Droubi, N.H. Faisal, Analysis of Acoustic Emission Propagation in Metal-to-Metal Adhesively Bonded Joints, J Nondestr Eval 37 (2018) 33, https://doi.org/10.1007/s10921-018-0488-y.

[31] J. Manterola, M. Aguirre, J. Zurbitu, J. Renart, A. Turon, I. Urresti, Using acoustic emissions (AE) to monitor mode I crack growth in bonded joints, Eng Fract Mech 224 (July 2019) (2020) 106778, https://doi.org/10.1016/j.engfracmech.2019.106778.

[32] M. Saeedifar, M.N. Saleh, S.T. De Freitas, D. Zarouchas, Damage characterisation of adhesively-bonded Bi-material joints using acoustic emission, Compos B Eng 176 (2019) 107356, https://doi.org/10.1016/j.compositesb.2019.107356.

[33] R.A.A. Lima, M. Drobiazko, A. Bernasconi, M. Carboni, On crack tip localisation in quasi-statically loaded, adhesively bonded double cantilever beam specimens by acoustic emission, Theor Appl Fract Mec 118 (2022) 103286, https://doi.org/10.1016/j.tafmec.2022.103286.

[34] F. Pashmforoush, M. Fotouhi, M. Ahmadi, Acoustic emission-based damage classification of glass/polyester composites using harmony search k-means algorithm, J. Reinf. Plast. Compos. 31 (10) (2012) 671–680, https://doi.org/10.1177/0731684412442257.

[35] W. Roundi, A. El Mahi, A. El Gharad, J.L. Rebiere, Acoustic emission monitoring of damage progression in Glass/Epoxy composites during static and fatigue tensile tests, Appl Acoust 132 (2018) 124–134, https://doi.org/10.1016/j.apacoust.2017.11.017.

[36] V. Carvelli, A. D'Ettorre, S.V. Lomov, Acoustic emission and damage mode correlation in textile reinforced PPS composites, Compos Struct 163 (2017) 399–409, https://doi.org/10.1016/j.compstruct.2016.12.012.

[37] S. Huguet, N. Godin, R. Gaertner, L. Salmon, D. Villard, Use of acoustic emission to identify damage modes in glass fibre reinforced polyester, Compos Sci Technol 62 (10–11) (Aug. 2002) 1433–1444, https://doi.org/10.1016/S0266-3538(02)00087-8.

[38] M. Carboni A. Bernasconi "Acoustic Emission Based Monitoring of Fatigue Damage in CFRP-CFRP Adhesive Bonded Joints", European Workshop on Structural Health Monitoring: Special Collection of, Papers-Volume 1 Springer International Publishing 2021 2020 10.1007/978-3-030-64594-6_59.

[39] D.E. Mouzakis, D.G. Dimogianopoulos, Acoustic emission detection of damage induced by simulated environmental conditioning in carbon fiber reinforced composites, Eng Fract Mech 210 (April 2018) (2019) 422–428, https://doi.org/10.1016/j.engfracmech.2018.04.037.

[40] W. Li, Y. Liu, P. Jiang, F. Guo, and J. Cheng, "Study on Delamination Damage of CFRP Laminates Based on Acoustic Emission and Micro Visualization," *Materials*, vol. 15, no. 4, Feb. 2022, doi: 10.3390/ma15041483.

[41] A. Ruairidh, Defect Detection and Condition Assessment of Adhesively-Bonded Joints Using Acoustic Emission, PhD Dissertation (2021).

[42] J. Kupski, S. Teixeira de Freitas, D. Zarouchas, P.P. Camanho, R. Benedictus, Composite layup effect on the failure mechanism of single lap bonded joints, Compos Struct 217 (2019) 14–26, https://doi.org/10.1016/J.COMPSTRUCT.2019.02.093.

[43] "HexPly ® 8552 Epoxy matrix (180°C/356°F curing matrix)," 2020.

[44] S. Teixeira de Freitas, D. Zarouchas, J.A. Poulis, The use of acoustic emission and composite peel tests to detect weak adhesion in composite structures, J Adhesion 94 (9) (2018) 743–766, https://doi.org/10.1080/00218464.2017.1396975.

[45] J. Kupski, D. Zarouchas, S. Teixeira de Freitas, Thin-plies in adhesively bonded carbon fibre reinforced polymers, Compos B Eng 184 (2020) 107627, https://doi.org/10.1016/j.compositesb.2019.107627.

[46] K. Ono, Calibration of acoustic emission sensors, Materials 508 (2016), https://doi.org/10.3390/ma9070508.

[47] K. Ono, H. Suzuki, T. Kinjo, Y. Hayashi, M. Takemoto, and K. Ono With Appendix, "Wavelet transform of acoustic emission signals Ancient metals View project Wavelet Transform of Acoustic Emission Signals," 1996, Accessed: May 06, 2022. [Online]. Available: https://www.researchgate.net/publication/284701251.

[48] K. Panasiuk, L. Kyzioł, K. Dudzik, The use of acoustic emission signal (AE) in mechanical tests, Przeglad Elektrotechniczny 95 (11) (2019) 8–11, https://doi.org/10.15199/48.2019.11.03.

[49] S. Kalafat, M.G. Sause, Acoustic emission source localisation by artificial neural networks, Struct Health Monit 14 (6) (2015) 633–647, https://doi.org/10.1177/1475921715607408.

[50] E. Pomponi, A. Vinogradov, A real-time approach to acoustic emission clustering, Mech Syst Signal Process 40 (2) (2013) 791–804, https://doi.org/10.1016/j.ymssp.2013.03.017.

[51] W. Zhou, W.-Z. Zhao, Y.-N. Zhang, Z.-J. Ding, Cluster analysis of acoustic emission signals and deformation measurement for delaminated glass fiber epoxy composites, Compos Struct 195 (2018) 349–358, https://doi.org/10.1016/j.compstruct.2018.04.081.

[52] D. Crivelli, M. Guagliano, A. Monici, Development of an artificial neural network processing technique for the analysis of damage evolution in pultruded composites with acoustic emission, Compos B Eng 56 (2014) 948–959, https://doi.org/10.1016/j.compositesb.2013.09.005.

[53] C. Barile, C. Casavola, G. Pappalettera, V. Paramsamy Kannan, Laplacian score and K-means data clustering for damage characterisation of adhesively bonded CFRP composites by means of acoustic emission technique, Appl. Acoust. 185 (2022) 108425, https://doi.org/10.1016/j.apacoust.2021.108425.

[54] L.B. Andraju, G. Raju, Damage characterisation of CFRP laminates using acoustic emission and digital image correlation: Clustering, damage identification and classification, Eng Fract Mech 277 (Jan. 2023), https://doi.org/10.1016/j.engfracmech.2022.108993.

[55] S. Patsias, W.J. Staszewski, Damage detection using optical measurements and wavelets, Struct Health Monit 1 (1) (2002) 5–22, https://doi.org/10.1177/147592170200100102.

[56] K.M. Bak, K. Kalaichelvan, G.K. Vijayaraghavan, B. Sridhar, Acoustic emission wavelet transform on adhesively bonded single-lap joints of composite laminate during tensile test, J Reinf Plast Compos 32 (2) (Oct. 2012) 87–95, https://doi.org/10.1177/0731684412459249.

[57] D. Biagini, J.A. Pascoe, R. Alderliesten, Investigation of compression after impact failure in carbon fiber reinforced polymers using acoustic emission, J Compos Mater 57 (10) (May 2023) 1819–1832, https://doi.org/10.1177/00219983231163853.

[58] M. Saeedifar, M.A. Najafabadi, D. Zarouchas, H.H. Toudeshky, M. Jalalvand, Clustering of interlaminar and intralaminar damages in laminated composites under indentation loading using Acoustic Emission, Compos B Eng 144 (March) (2018) 206–219, https://doi.org/10.1016/j.compositesb.2018.02.028.

[59] F.E. Oz, N. Ersoy, S.V. Lomov, Do high-frequency acoustic emission events always represent fibre failure in CFRP laminates? Compos Part A Appl Sci Manuf 103 (2017) 230–235, https://doi.org/10.1016/j.compositesa.2017.10.013.

[60] M. Saeedifar, M. Fotouhi, M. Ahmadi Najafabadi, H. Hosseini Toudeshky, Prediction of delamination growth in laminated composites using acoustic emission and Cohesive Zone Modeling techniques, Compos Struct 124 (2015) 120–127, https://doi.org/10.1016/j.compstruct.2015.01.003.

[61] J.A. Pascoe, R.C. Alderliesten, R. Benedictus, Methods for the prediction of fatigue delamination growth in composites and adhesive bonds - A critical review, Eng

Fract Mech 112–113 (2013) 72–96, https://doi.org/10.1016/j.engfracmech.2013.10.003.
[62] F. Lissek, A. Haeger, V. Knoblauch, S. Hloch, F. Pude, M. Kaufeld, Acoustic emission for interlaminar toughness testing of CFRP: Evaluation of the crack growth due to burst analysis, Compos B Eng 136 (2018) 55–62, https://doi.org/10.1016/j.compositesb.2017.10.012.
[63] R. Mohammadi, M. Ahmadi Najafabadi, H. Saghafi, M. Saeedifar, and D. Zarouchas, "A quantitative assessment of the damage mechanisms of CFRP laminates interleaved by PA66 electrospun nanofibers using acoustic emission," *Compos Struct*, vol. 258, 2021, doi: 10.1016/j.compstruct.2020.113395.
[64] A.J. Brunner, Correlation between acoustic emission signals and delaminations in carbon fiber-reinforced polymer-matrix composites: A new look at mode I fracture test data, in: 32nd European Conference on Acoustic Emission, 2016, pp. 55–64.
[65] I.J. Baran, M.B. Nowak, J.P. Chłopek, K.J. Konsztowicz, Acoustic Emission from Microcrack Initiation in Polymer Matrix Composites in Short Beam Shear Test, J Nondestr Eval 37 (1) (2018) 1–10, https://doi.org/10.1007/s10921-017-0455-z.
[66] F. Awaja, S. Zhang, M. Tripathi, A. Nikiforov, N. Pugno, Cracks, microcracks and fracture in polymer structures: Formation, detection, autonomic repair, Prog Mater Sci 83 (2016) 536–573, https://doi.org/10.1016/j.pmatsci.2016.07.007.
[67] A.J. Kinloch, J.H. Lee, A.C. Taylor, S. Sprenger, C. Eger, D. Egan, Toughening structural adhesives via nano-and micro-phase inclusions, J Adhesion 79 (2010) 867–873, https://doi.org/10.1080/00218460309551.
[68] R. Lopes Fernandes, S. Teixeira de Freitas, M. K. Budzik, J. A. Poulis, and R. Benedictus, "From thin to extra-thick adhesive layer thicknesses: Fracture of bonded joints under mode I loading conditions," *Eng Fract Mech*, vol. 218, Sep. 2019, doi: 10.1016/J.ENGFRACMECH.2019.106607.